Transient Oxygen Droplet Combustion in a Hydrogen Atmosphere: A Numerical Approach

Jonathan Frydman

A thesis
submitted in partial fulfillment of the
requirements for the degree of

Master of Science in Aeronautics & Astronautics

University of Washington

2018

Committee:

Professor James Hermanson

Ass. Professor Antonino Ferrante

Program Authorized to Offer Degree:
Aeronautics & Astronautics

University of Washington

Abstract

Transient Oxygen Droplet Combustion in a Hydrogen Atmosphere: A Numerical Approach

Jonathan Frydman

Chair of the Supervisory Committee:
Professor James Hermanson
Aeronautics & Astronautics

In liquid rocket propulsion oxygen normally enters the combustion chamber as a dispersed phase, as the hydrogen fuel more rapidly evaporates into a continuous, vapor phase. The foundational configuration considered here is a single liquid oxygen droplet surrounded by gaseous hydrogen. This project employs computational techniques to model the coupled oxidizer/fuel mixing, ignition, and combustion behaviors of the liquid oxygen/gaseous hydrogen system. For simplicity the problem is modeled with spherical symmetry, consistent with microgravity conditions.

Conservation equations are implemented within the OpenFOAM platform to calculate species concentrations, temperatures, and heat release rates as functions of time and space. The OpenFOAM software package allows for calculations to be run in a sophisticated runtime environment. Both single-step and six-step chemical reaction models are employed for simulating oxygen-hydrogen combustion. Numerical simulations of both chemical models show diffusion, ignition, and the subsequent formation of three distinct flame zones. These include premixed flames in both the fuel and oxidizer sides of the diffusion flame at the stoichiometric interface. The premixed flame zones weaken as a quasi-steady combustion state is achieved in both cases. The global-chemistry reaction simulation is run until near total consumption of the oxygen occurs. A number of suggestions are presented based off these results for improving future simulation accuracy and efficiency.

TABLE OF CONTENTS

LIST OF FIGURES

LIST OF TABLES

NOMENCLATURE

A: Arrhenius equation pre-exponential

c: Molar concentration

c_p: Isobaric specific heat capacity (per unit mass)

c_p: Isochoric specific heat capacity (per unit mass)

C_p: Isobaric total heat capacity

$\mathcal{D}$: Molar diffusivity

h: Specific enthalpy (per unit mass)

h_f: Specific enthalpy of formation (per unit mass)

H: Total Enthalpy

$\mathcal{H}$: Heaviside step function

k: Temperature dependence of the reaction rate

KE: Total kinetic energy

Le: Lewis Number

m: Mass

M: Molecular mass

P: Thermodynamic pressure

Pr: Prandtl number

$\vec{q}$: Heat flux density

$\dot{Q}$: Heat production rate

R: Source of specie density due to chemical interactions

R_u: Universal gas constant

R_{gas}: Specific gas constant

RR: Reaction rate

Ss: Schmidt number

T: Absolute Temperature

T_a: Activation Temperature

$\vec{u}$: Velocity vector

U: Total internal energy

v: Specific volume

$\forall$: Total volume

X: Mass fraction

Y: Mole fraction

Z: Compressibility

α: Heat diffusivity

β: Temperature exponential of the modified Arrhenius equation

δ: Dirac delta function

Θ: Boiling/ Phase-change temperature

κ: Thermal conductivity

μ: Dynamic viscosity

ν: Stoichiometric coefficient

ρ: Density

τ: Deviatoric stress tensor

Φ: Energy Dissipation function

ψ: Ignition strength

∂_t: Time derivative

$\vec{\nabla}$: Gradient

$\vec{\nabla}\cdot$: Divergence

$\otimes$: Outer product

ACKNOWLEDGMENTS

The author wishes to express sincere appreciation to University of Washington, and the department of Aeronautics and Astronautics, where he has had the opportunity to work with a number of supportive peers and elucidative mentors. A specific thank-you goes Professor to James Hermanson for the research guidance, project direction, and draft edits that went into writing this thesis.

Chapter 1

INTRODUCTION

1.1 Liquid Rocket Propulsion

Liquid Oxygen/ Hydrogen (LOX/H2) rockets play a vital role in the technological repository of space flight. This bi-propellant combination provides the high specific impulse and thrust levels required for space travel, while only producing harmless water as exhaust. High performance, low risk, and moderate cost of this fuel combination places H2-LOX as one of the most attractive rocket propellants for space-travel. As such developing a comprehensive model for H2-LOX combustion in rockets would provide great benefit towards developing rocket combustion chambers.

Due to lack of a full model combustion transients are often overlooked in rocket engines in favor of achieving rapid steady state performance[1]. Furthermore contemporary analysis is unable to explain how combustion effects the higher resonant acoustic modes within combustion chambers[2]. Due to the massive expense required in developing and testing empirical models for the many variable permutations, many aspects of combustion chamber design have been canonized as rule-of-thumb [3][1]. Designs outside the established prove to be monetarily risky. A functional model for the combustion-acoustic modeling would greatly mitigate these costs and risks associated with design testing.

The risk associated with operating rockets in unsteady combustion regimes limits potential applications. Rocket throttling can be used to maximize thrust throughout the range of atmospheric conditions experienced during atmospheric climb, however certain care needs to be taken not to trigger combustion chamber resonance when traversing performance states. Pulsed altitude thrusters provide small space craft fine control and high thrust during descent operations but combustion transients limit the minimum length of each pulse of their

chemical thrusters. Thus by generating an increased understand of rocket combustion transients, an increasing number of propulsion tactics become available. With more propulsion techniques available, various space missions become increasingly feasible.

1.2 Fuel Injection & Droplet Formation

The research proposed here applies to this domain in LOX/H2 rockets: the region of fuel/oxidizer injection, where oxidizer droplet vaporization and combustion commences. While liquid hydrogen is typically carried in missions involving LOX, hydrogen more readily vaporizes, hence the focus on the gas-liquid, two-phase scenario.

A wide variety of fluid conditions exist in the near injector regime. Depending on droplet size, combustion may vary from near-equilibrium to near-extinction iii . Chugging and other instabilities may result from poor distribution or extreme local variations of these regions. Further research into the vaporization and diffusion of LOX droplet and gaseous H2 combustion include formation and distribution of combustion products, as well as local variation of liquid/ gas properties. This research proposes to investigate the full formation and distribution of combustion products and thermal energy within ideal gas approximation.

In order to build a solid foundation of combustion behavior, isolated LOX droplets will be studied within a microgravity environment, such as one found during the space shuttle missions. While real rockets exhibit moment dominated flows, this kinetic simplification provides an essential stepping stone into building a full working model of near injector combustion.

1.3 Goals and Objectives

In order to accomplish the overall objective of modeling the vaporization and combustion of a liquid oxygen droplet in gaseous hydrogen, the following sub-objectives have been identified:

1. Establish the use of the OpenFOAM numerics package for modeling oxygen/hydrogen combustion under cryogenic conditions, using both global-reaction, and reduced-order

chemistry.

2. Deconstruct the method used by the prepackeged solvers within OpenFOAM to understand modern techniques used for computational combustion.

3. Modify OpenFOAM code to add ignition capabilities

4. Identify solver parameters and settings to capture transient ignition behaviors

5. Use simulated combustion results of global and reduced order chemistry to estimate:

    - Droplet lifetime
    - Flame temperatures
    - Flame locations and structure
    - Specie distributions

6. Critique the numerical model used by OpenFOAM and present suggestions for future modeling of LOX/H2 droplet combustion.

The following chapters will introduce the mathematics, decouple the individual phenomena, address the numerical methods, present results, and explain the dynamics captured in droplet combustion.

Chapter 2

PROBLEM STATEMENT

In order to give mathematical rigor to the simulation of oxygen droplet combustion, this chapter gives the mathematical description of the equations being solved and the coefficients defined. All species are modeled as calorically perfect, ideal gases. Many of these equations were picked due to combination of the OpenFOAM solvers/ models and requirements on capturing combustion physics. General derivations were also found in various OpenFOAM supporting material [4][5][6].

2.1 Partial Differential Equations

The partial differential equations (PDEs) driving the transport of mass, momentum, species, and energy are rooted in fundamental conservation laws. A few approximations and limitations are made to them according to OpenFOAM limitations, which are noted following the equation.

2.1.1 Conservation of Mass

$$\partial_t \rho + \vec{\nabla} \cdot (\rho \vec{u}) = 0 \tag{2.1}$$

2.1.2 Conservation of Momentum

$$\partial_t (\rho \vec{u}) + \vec{\nabla} \cdot (\rho \vec{u} \otimes \vec{u}) = -\vec{\nabla} P - \vec{\nabla} \cdot \tau \tag{2.2}$$

For a Newtonian fluid:

$$\vec{\nabla} \cdot \tau = -\vec{\nabla} \cdot \left[\mu \big(\vec{\nabla} \vec{u} + (\vec{\nabla} \vec{u})^T \big) \right] + \vec{\nabla} \left[\frac{2}{3} \mu \big(\vec{\nabla} \cdot \vec{u} \big) \right] \tag{2.3}$$

2.1.3 Conservation of Species

$$\partial_t(\rho Y_i) + \vec{\nabla} \cdot (\rho Y_i \vec{u}_i) - \vec{\nabla} \cdot \left[\mathcal{D}_i \vec{\nabla}\big(\rho Y_i\big)\right] = R_i \tag{2.4}$$

Let the diffusivity of species i, $\mathcal{D}_i$, be approximated through a unity Schmidt number:

$$Sc_i = \frac{\nu}{\mathcal{D}_i} \approx 1 \quad \Rightarrow \quad \mathcal{D}_i = \nu \tag{2.5}$$

Since the bulk fluid can be assumed to be in kinetic equilibrium, e.g.

$$\vec{u}_i = \vec{u} \tag{2.6}$$

no species momentum transport need be accounted for.

2.1.4 Conservation of Energy

$$\partial_t(\rho h + \frac{1}{2}\rho|\vec{u}|^2) + \vec{\nabla} \cdot \left[\rho\vec{u}\big(h + \frac{1}{2}|\vec{u}|^2\big)\right] - \partial_t P - \vec{\nabla} \cdot \big(\kappa\vec{\nabla}T\big) = \dot{Q}_{rxn} + \dot{Q}_{ign} \tag{2.7}$$

Let the heat conductivity of the fluid, κ, be approximated through a unity Prandtl number:

$$Pr = \frac{\nu}{\alpha} \approx 1 \quad \Rightarrow \quad \kappa = c_p\mu \tag{2.8}$$

2.2 Chemical Sources

The following equations connect the PDE's to the chemistry involved in combustion, as well as the user-specified ignition source.

2.2.1 Reaction Rate

$$RR_j = k_j \prod_{l}^{N_{species}} c_l^{\nu_{j,l}} \tag{2.9}$$

The reaction rate above is proportional to concentration factors as well as the rate factor, k, determined through the modified irreversible Arrhenius equation:

$$k_j = A_j T^{\beta_j} e^{-\frac{T_{a,j}}{T}} \tag{2.10}$$

2.2.2 PDE Source Terms

$$R_i = -\sum_{j}^{N_{rxn}} \nu_{i,j} RR_j \tag{2.11}$$

$$Q_{rxn} = \sum_{j}^{N_{rxn}} \left(RR_j \sum_{l}^{N_{species}} \nu_{j,l} h_{f,l} \right) \tag{2.12}$$

$$Q_{ign} = \begin{cases} h(1+\psi_{strength}) & \text{for } t_{ign,start} < t \leq t_{ign,end} \quad \& \quad r \in IgnLocations \\ 0 & \text{otherwise} \end{cases} \tag{2.13}$$

2.3 Equations of State

The equations of state are necessary to link the conservation laws to each other in what is typically known as the "closure problem."

$$P = cR_uT \tag{2.14}$$

$$c = \rho \sum_{i}^{N_{species}} \frac{Y_i}{M_i} \tag{2.15}$$

$$h = h_f + c_pT \tag{2.16}$$

$$c_p = \frac{5}{2} R_u \sum_{i}^{N_{species}} \frac{Y_i}{M_i} \tag{2.17}$$

2.4 Chemistry

The combustion process includes a number individual chemical reactions, also known as steps. While theoretically there are a large quantity of participating reactants in $H_2 - O_2$ combustion, only eight appear in measurable quantity. They are:

- H_2 - Hydrogen
- O_2 - Oxygen
- H_2O - Water

- H - Hydrogen radical
- O - Oxygen radical
- OH - Hydroxyl *or* Hydroxide radical
- HO_2 - Hydroperoxyl *or* Perhydroxy radical
- H_2O_2 - Hydrogen peroxide

A 21-step model involving these reactants can fully capture the chemical dynamics[7]. Due to the computational intensity of tracking all species and reactions, chemistry was simplified by reducing the number of participants and reactions into two numerically less expensive models:

- 3 Participants & 1 Reaction
- 6 Participants & 6 Reactions

Hydroperoxyl and hydrogen peroxide are neglected in both cases. Helium gas is introduced as a dilutant and is a by-standard species rather than a participant. This section shows the chemistry involved in both reduced order models as well as the coeffecient values[1][2] used for Equation 2.10.

2.4.1 Single Step Chemistry

The single-step chemistry model used in this report was obtain from the highly popular model developed at Lawrence Livermore National Lab, CA[8].

---

[1]The form of the modified Arrhenius equation applied in the chemistry uses the OpenFOAM expression (see Equation 2.10). As such the reported values of Ta are those found in the respective source divided by the universal gas constant value.

[2]Units of A varies based on reaction order and temperature dependence. $A[=](\frac{mol}{m^3})^{1-\sum \nu_r eactants} K^{-\beta}$. Units for the activation temperature, Ta, are in Kelvin.

N_{rxn}	1
$N_{species}$	4
Species	O_2, H_2, H_2O, He

Table 2.1: Overview of the single step chemistry model.

Reactions	A[1]	Ta	β	ν_{O2}	ν_{H2}	ν_{H2O}	ν_{He}
$H_2 + \frac{1}{2}O_2 \Rightarrow H_2O$	1.8e13	17614	0	0.5	1	-1	0

Table 2.2: Single step chemistry reaction, Arrhenius parameters, and stoichiometric coefficients.

2.4.2 Six Step Chemistry

The following reactions are part of the full 21 reaction model and selected based off their roles of initiating, chain-branching, and chain-terminating roles. The reactions are taken from Table-C1 of *Combustion*[7].

N_{rxn}	6
$N_{species}$	7
Species	O_2, H_2, H_2O, O, H, OH, He

Table 2.3: Overview of the six-step chemistry model.

2.5 Material Properties

The material properties of the species appear as coefficients in PDE's shown previously. As such proper definition is important. The assumptions on the Schmidt and Prandtl numbers allow for the fluid to be described through Sutherland's viscosity law. Note that the viscosity coefficients come from the defaults values found in OpenFOAM's ChemkinToFoam utility.

Reactions	A	Ta	β	ν_{O2}	ν_{H2}	ν_{H2O}	ν_{O}	ν_{H}	ν_{OH}	ν_{He}
$H + O_2 \Rightarrow O + OH$	3.55e15	8353	-0.4	1	0	0	-1	1	-1	0
$O + H_2 \Rightarrow H + OH$	5.08e04	3166	2.7	0	1	0	1	-1	-1	0
$H_2 \Rightarrow 2H$	4.58e19	52530	-1.4	0	1	0	0	-2	0	0
$H + OH \Rightarrow H2O$	3.80e22	0	-2.0	0	0	-1	0	1	1	0
$2O \Rightarrow O_2$	6.16e15	0	-0.5	-1	0	0	2	0	0	0
$H_2 + OH \Rightarrow H + H2O$	2.16e08	1726	1.5	0	1	-1	0	-1	1	0

Table 2.4: Six step chemistry reactions, Arrhenius parameters, and stoichiometric coefficients.

For reference, the viscosity of helium[9] is rough twice the value described by Equations 2.18.

$$\mu = \text{1.67212e-6 Pa-s}\frac{T^{1.5}}{T + 170.672K} \tag{2.18}$$

All else needed are the appropriate molar masses and heats of formations of the species.

Species	M $[\frac{kg}{kmol}]$	$h_f[\frac{J}{kg}]$
O_2	31.9988	0
H_2	2.016	0
H_2O	18.0153	-13423.4
O	15.9994	15574
H	1.00794	216281
OH	17.00734	2293
He	4.0026	0

Table 2.5: Table of molecular weights and heats of formation.

Chapter 3

FUNDAMENTAL PROCESSES DECOUPLED

Droplet combustion exhibits complex interactions arising from the coupled conservation properties and fluid dynamic phenomena. As such analyzing combustion simulation results can be quite challenging. The following thought experiments serve as lenses with which to elucidate the basic mechanisms at play. By separating each effect, analysis becomes less cumbersome. With a clear perspective on the phenomena, simulation results can be transformed into conclusions via the interlinking of the decoupled processes.

This chapter presents a simplified scenario for each of the main mechanisms, evaporation, diffusion, ignition, and combustion. The math and models presented reflect either computer simulation or hypothesized real mechanisms. Each section acts independently to establish ideas and possibilities about droplet combustion.

3.1 Phase Transition as a Continuum (Evaporation)

Michael Faraday shows in his written lectures, "A Chemical History of a Candle," how the solid wax of a candle does not burn directly but first is vaporized by the nearby flame. The wax vapors then travel into the flame where they are burned and produce more heat, continuing the vaporization of the candle further [10]. Such is the case with the oxygen droplet, though the oxidizer is now the vaporizing component.

The evaporation of liquid oxygen into the gaseous phase adds a complication to modeling droplet combustion. The most direct way to account for the effects of both phases would be to model each individually, however this adds computational complexity where it may not be necessary. For a small fixed volume containing mixed phases, net extensive fluid properties can be obtained via the addition of extensive properties of both phases. A composite intensive

definition of the mixed phase can be constructed by dividing net extensive properties by the volume. This is effectively an average. Since intensive properties are defined through state variables, so too can this mixed volume, assuming thermal and kinetic equilibrium. Properties such as viscosity, conductivity, density, and heat capacity can then be defined as functions of temperature with the phase transition effects incorporated via additional source terms. As such a single phase, imaginary fluid can mimic the properties of liquid and vapor oxygen in equilibrium.

With the goal of constructing composite descriptions of a substance undergoing a liquid-gas transition in mind, certain questions must be answered. How can phases be described from a macroscopic perspective? Liquids typically differ from perfect gases in their compressibility. A homogeneous liquid is essentially incompressible and thus constant density. Perfect gases are governed by the ideal gas law. While these descriptions work for perfect/ ideal states, real substances have more complicated behavior.

The equation of state for real gases can be defined through the compressibility equation:

$$\frac{P}{\rho RT} = Z(T, P) \tag{3.1}$$

By defining Z as a ratio of pressure to temperature, the density becomes constant and thus this compressibility represents an "incompressible real gas."

$$Z = \frac{P}{\rho_0 RT} \quad \Rightarrow \quad \rho = \rho_0 \tag{3.2}$$

For an ideal gas Z equals unity, so by defining compressibility as a piecewise function, the equation of state for a continuous fluid can be expressed as:

$$Z(T, P) = \begin{cases} \frac{P}{\rho_0 RT} & \text{for } T < T_{evap}(P) \\ 1 & \text{for } T \geq T_{evap}(P) \end{cases} \tag{3.3}$$

where $T_{evap}(P)$ is the evaporation temperature for oxygen as a function of pressure. The first piece represents the liquid state of the fluid and the second piece represents the gas. Equation 3.3 demonstrates a composite equation of state for the fictitious fluid describing both the liquid an gas phases of a transitioning fluid.

This technique of defining piecewise properties can be extended to the rest of the material properties. For an evaporating droplet, the total pressure of the vapor immediately surrounding the liquid droplet is on the same order of magnitude as the droplet interior pressure. As such conductivity, dynamic viscosity, and heat capacity are nominally functions of temperature. For example thermal conductivity:

$$\kappa(T) = \begin{cases} \kappa_{liq}(T) & \text{for } T < T_{evap}(P) \\ \kappa_{gas}(T) & \text{for } T \geq T_{evap}(P) \end{cases} \tag{3.4}$$

and dynamic viscosity:

$$\mu(T) = \begin{cases} \mu_{liq}(T) & \text{for } T < T_{evap}(P) \\ \mu_{gas}(T) & \text{for } T \geq T_{evap}(P) \end{cases} \tag{3.5}$$

As an aside the liquid viscosity can be modeled as exponentially decreasing,

$$\mu_{liq}(T) = N_A \hbar \rho M_W e^{0.408 \frac{\triangle \tilde{U}_{vap}}{R_u T}} \tag{3.6}$$

where $\triangle \tilde{U}_{vap}$ is the internal energy of vaporization [11][1]. The gaseous viscosity can be modeled using the Sutherland formula:

$$\mu_{gas}(T) = \frac{A_s T^{1.5}}{T + T_s} \tag{3.7}$$

where A_s and T_s are empirical coefficients for a gas. [12]

Heat capacity follows the same piecewise pattern with an added caveat: the latent heat of vaporization must be considered. The enthalpy of a real gas held at constant pressure, which undergoes no phase change from 0 Kelvin to some temperature T^* can be defined as:

$$H(T) = H_f^o + \int_0^{T^*} C_p(T) dT \tag{3.8}$$

where H_f^o is the standard heat of formation. If this gas changes phase (or structure) at some temperature Θ below the designated T^*, integration is split up into two regions, below and

[1]See equation 1.5-10 in [11] for a slightly modified form of Equation 3.6

above Θ, and the additional heat of formation term is added as follows:

$$H(T) = H_f^o + H_{xfm} + H_{phase1} + H_{phase2} \tag{3.9}$$

$$= H_f^o + H_{xfm} + \int_0^{\Theta} C_{p,phase1}(T)dT + \int_{\Theta}^{T^*} C_{p,phase2}(T)dT \tag{3.10}$$

where H_xfm is the heat of transformation. This quantity can be re-expressed as a convolution with the Dirac delta function centered at Θ. Since the integrand of the convolution evaluates to zero everywhere but $T = \Theta$, the integration bounds can be changed to $[0, T^*]$.

$$H_{xfm} = \int_{-\infty}^{\infty} H_{xfm}\delta(T-\Theta)dT = \int_0^{T^*} H_{xrm}\delta(T-\Theta)dT \tag{3.11}$$

The enthalpy contributions from each phase can be manipulated in a similar way using the Heaviside function:

$$H_{phase1} = \int_0^{T^*} C_{p,phase1}(T)\Big(1 - \mathcal{H}(T-\Theta)\Big)dT \tag{3.12}$$

$$H_{phase2} = \int_0^{T^*} C_{p,phase1}(T)\mathcal{H}(T-\Theta)dT \tag{3.13}$$

Before combining equations 3.11-3.13, define an agglomerated heat capacity, C_p^* such that:

$$C_p^*(T) = \begin{cases} C_{p,phase1}(T), & \text{for } T < \Theta \\ H_{xfm}\delta(T-\Theta), & \text{for } T = \Theta \\ C_{p,phase2}(T), & \text{for } T > \Theta \end{cases} \tag{3.14}$$

From here the enthalpy can be expressed in a single phase fashion:

$$H(T) = H_f^o + \int_0^{T^*} C_p^*(T)dT \tag{3.15}$$

Through this method of piecewise agglomeration, material properties for oxygen in both liquid and gas phase can be incorporated into simulation as if a single phase. The compressible equation of state links the transition in not only a mathematical manner but conceptual as well.

3.2 Keyhole Diffusion of Heat and Mass (Diffusion)

The flow of heat is typically characterized by its diffusive nature, but how does the introduction of species diffusion affect this mechanism? Combined heat and mass diffusion is neither a clear case of conduction nor convection. The two mechanism determine the temperature profile driving the reaction of hydrogen and oxygen. While it is clear that temperature can be effected by heat transfer, mass transport also plays an important role.

It is paramount to understand the relative effect of each phenomena especially when analyzing experimental and numerical results. The analytical derivation presented in this chapter will give context to the limitations of modeling employed. A finite-volume-style derivation is applied in this section to a one dimensional scenario but the mathematics are generalized to hold in three dimensions. The results of this derivation can be further linked to experimentally based material properties or kinetic theory based descriptions.

In the finite volume method, each cell acts as an open system. The temperature of the cell is not only affected by the heat transfer at the boundaries but also by the mass flux. Which is the dominating factor in droplet combustion? Suppose that a 100% oxygen gas environment meets a pure hydrogen gas reservoir through a keyhole with some depth d. Oxygen fills one half of the channel depth and hydrogen occupies the other half. Initially everything is at some ambient temperature T_∞ and the resulting diffusion and heat transport processes are slow enough to assume isobaric behavior, occurring at P_∞. Figure 3.1 shows a schematic.

Application of the 1^{st} Law of Thermodynamics will resolve the temperature around both the oxygen and hydrogen halves of the keyhole due to mass transport. For brevity the oxygen volume, $C\not{V}_{O2}$, will be considered. Neglecting any bulk fluid flow gradients or reactions:

$$\partial_t H = H_{in} - H_{out} = -\oint_{\partial C\not{V}} \sum_i \rho_i h_i \vec{v}_i \cdot d\vec{A} \tag{3.16}$$

where $\vec{A}$ is the area vector associated with the openings of $C\not{V}_{O2}$ and by default points outwards. $\vec{v}_i$ is the speed at which species i flows. The speed and density can be replaced

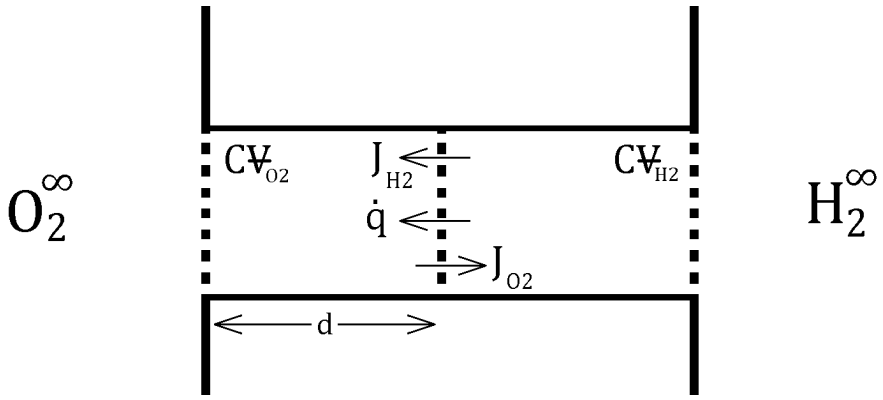

Figure 3.1: Schematic of a one-dimensional, multi-species, heat-mass transfer problem. Two control volumes are shown with mass fluxes into each other and one heat flux between the two.

by the molar flux density, $\vec{J_i}$, which can intern be replaced by Fick's Law of diffusion.

$$\rho_i \vec{v_i} = M_i \vec{J_i} \tag{3.17}$$

$$\vec{J_i} = -\mathcal{D}_{i,j} \vec{\nabla} c_i \tag{3.18}$$

where, M_i is the molecular weight of species i and $\mathcal{D}_(i,j)$ is the diffusion coefficient between species i and j. c_i is the molar concentration [13]. Combining Equations 3.16, 3.17, and 3.18:

$$\partial_t H = \oint_{\partial C\forall} \sum_i h_i M_i \mathcal{D}_{i,j} \vec{\nabla} c_i \cdot d\vec{A} \tag{3.19}$$

In the following steps applying the divergence theorem, expressing total enthalpy as a integral of volumetric enthalpy, applying Leibniz's integral rule for a static boundary, and letting $C\forall_{O2}$ approach a differential size leads to:

$$\partial_t H = \int_{C\forall} \vec{\nabla} \cdot \left(\sum_i h_i M_i \mathcal{D}_{i,j} \vec{\nabla} c_i \right) d\forall \tag{3.20}$$

$$= \partial_t \int_{C\forall} \rho h d\forall \tag{3.21}$$

$$= \int_{C\forall} \partial_t (\rho h) d\forall \tag{3.22}$$

$$\Rightarrow \partial_t(\rho h) = \vec{\nabla} \cdot \left(\sum_i h_i M_i \mathcal{D}_{i,j} \vec{\nabla} c_i \right) \tag{3.23}$$

At this time Equation 3.23, which represents the accumulation due to species transport, can be superimposed with Fourier's law of heat conduction, to show accumulation of enthalpy due to combined heat and diffusive mass transport.

$$\partial_t(\rho h) = \vec{\nabla} \cdot \left(\sum_i h_i M_i \mathcal{D}_{i,j} \vec{\nabla} c_i + \kappa \vec{\nabla} T \right) \tag{3.24}$$

Equation 3.24 holds valid for general cases. The only assumptions build into the expression involves restrictions in the particle diffusion model of Fick's Law [13]. In order to step from an enthalpy transport equation to a temperature balance statement, a couple assumptions need to be made:

1. Negligible changes in volumetric heat capacity in space and time, i.e.:

$$\delta_t(\rho c_p) = |\vec{\nabla}(\rho c_p)| = 0 \tag{3.25}$$

2. Negligible total molar concentration gradient. I.e.:

$$|\vec{\nabla} c| = 0 \tag{3.26}$$

Assumption 1 allows for the volumetric heat capacity to be divided out. And since for a perfect gas, $h = c_p T$,

$$\partial_t T = \vec{\nabla} \cdot \left(\sum_i \frac{c_{p,i}}{\rho c_p} M_i \mathcal{D}_{i,j} T \vec{\nabla} c_i + \frac{\kappa}{\rho c_p} \vec{\nabla} T \right) \tag{3.27}$$

Assumption 2 allows for the species concentration gradient to be re,expressed as a mole fraction gradient, since $c_i = X_i c$. Furthermore let the total concentration, c, be replaced by the ratio of density to mean molecular mass in the cell, $c = \rho/M$.

$$\partial_t T = \vec{\nabla} \cdot \left(\sum_i \frac{c_{p,i} M_i}{c_p M} \mathcal{D}_{i,j} T \vec{\nabla} X_i + \frac{\kappa}{\rho c_p} \vec{\nabla} T \right) \tag{3.28}$$

Note that for a perfect gas the molecular heat capacity (per mole), $c_p M$, is equal to $2.5R_u$ regardless of species. This allows for the heat capacity and molecular weight terms to drop out to leave:

$$\partial_t T = \vec{\nabla} \cdot \left(\sum_i \mathcal{D}_{i,j} T \vec{\nabla} X_i + \frac{\kappa}{\rho c_p} \vec{\nabla} T \right) \tag{3.29}$$

Substituting in the heat diffusivity, α, as the coefficient acting on the gradient of temperature, allows for the definition of the non-dimensional inverse-Lewis number, Le^{-1}, as the ratio of heat diffusivity to mass diffusivity.

$$Le_i^{-1} = \frac{\mathcal{D}_{i,j}}{\alpha} \tag{3.30}$$

Finally,

$$\partial_t T = \vec{\nabla} \cdot \left[\alpha \left(\sum_i Le_i^{-1} T \vec{\nabla} X_i + \vec{\nabla} T \right) \right] \tag{3.31}$$

Equation 3.31 represents the heat and mass sources of temperature transport in a relative manner. Both gradient terms lead to diffusion but it is worth noting the temperature multiplier on the mole fraction gradient. Two scenarios with the same gradients but at different temperatures will see different dynamics. Mass diffusion makes a greater impact at higher temperatures.

The inverse Lewis number represents the relative time scales of heat diffusion vs mass diffusion. For example, fast mass diffusion or slow heat transfer will result in an inverse Lewis number of greater than unity. This scenario leads to mass flux dominating the effects of temperature change. Other values of the inverse Lewis number leads to different heating regimes.

The droplet combustion simulation reported in this paper does not use this end form of the first law for calculation, but the result from this derivation give insight into how the simulation performs against expected reality when certain constraints are placed on the Lewis number.

3.3 The Complications of Detonation (Ignition)

At near cryogenic temperatures, oxygen and hydrogen gases do not react. There is not enough molecular motion to surpass the activation energy thresholds needed for combustion. In order to start the chemical cascade, a source of energy must be provided. The simulations in this project introduces a spark in the fluid domain as a numerical source. The purpose of numerical ignition counter-intuitively is not to heat the region of application, but rather to manipulate the temperature profile near the droplet.

Ignition is presented in Equation 2.7 as an enthalpy/ kinetic energy source. Because of this the energy associated with the ignition can manifest in forms other than temperature increase. In the volumetric form this can be shown as:

$$H + KE = U + P\cancel{\forall} + \frac{1}{2}m|\vec{u}|^2 \tag{3.32}$$

$$= \cancel{\forall}\big(\rho c_v T + P + \frac{1}{2\rho}[\rho|\vec{u}|]^2\big) \tag{3.33}$$

$$\Rightarrow \frac{H + KE}{\cancel{\forall}} = \big(\rho c_v T + P + \frac{1}{2\rho}[\rho|\vec{u}|]^2\big) \tag{3.34}$$

The presence of additional, non temperature, terms in the above equation shows that ignition, as an enthalpy source, is not just a temperature source, but also a pressure and momentum source. On a differential time scale, the pressure couples to the local temperature through ideal gas law effects and so temperature spike immediately after ignition application. This temperature spike must be high enough to trigger the cascade the chemical reactions with sufficient exothermic net effects, or else combustion will not be sustained. Since pressure and momentum tend to advect out of fixed control volumes, ignition can cause propagating detonation waves. The resultant traveling waves hold part of the ignition source enthalpy.

3.4 Spherical Shock Tube (Waves)

As mentioned in the previous section, ignition may cause acoustic waves. This can be seen by linearizing the conservation of mass and momentum equations for density and pressure,

resulting with:

$$\partial_t^2 P' = \nabla^2 P' \tag{3.35}$$

Where P' represents the pressure differential with respect to some nominal value. For ignition applied to a point, waves will propagate radially outward, decreasing with strength as the wave travels away from the source point. For a spherical shell of ignition, as applied in numerical simulations due to symmetry conditions, something much different happens. Each point on the shell's surface acts as an individual ignition source. This leads to two spherical waves forming. One travels outwards radially, similarly to the point ignition, with wave strength diminishing. The other travels inwards, with progressively decreasing diameter but drastically increasing magnitude. The energy of the inward wave eventually meets at a point creating a pressure spike with an infinite value.

This infinite value occurring at the sphere center can be seen in the solution the the spherical Bessel function of the second kind. The acoustic wave equation can be broken down into a number of wave modes, denoted by k, at any point in time with each mode subject to the equation:

$$k^2 P' = \nabla^2 P' \tag{3.36}$$

This is the Helmholtz differential equation and has a solution of any combination of spherical Bessel functions, j_n and y_n, which are of the first and second kind respectively. Figure 3.2 shows the first three spherical Bessel functions of the second kind, displaying the discontinuity at the origin which approaches an infinite value. The detonation wave posed, can be expressed as a super position of these spherical Bessel functions at all points in time and can therefore posses the discontinuity at the origin as well.

The spherical-wave-propagation scenario also poses as a converging nozzle with a zero valued exit area. The spherical symmetry of a shell ignition causes no fluxes perpendicular to the radius, similar to the walls of a nozzle. These symmetry walls guide a flow through the nozzle, ever increasing the speed as the cross sectional area decreases. Once there is no more area the velocity diverges, becoming infinite, as does the pressure.

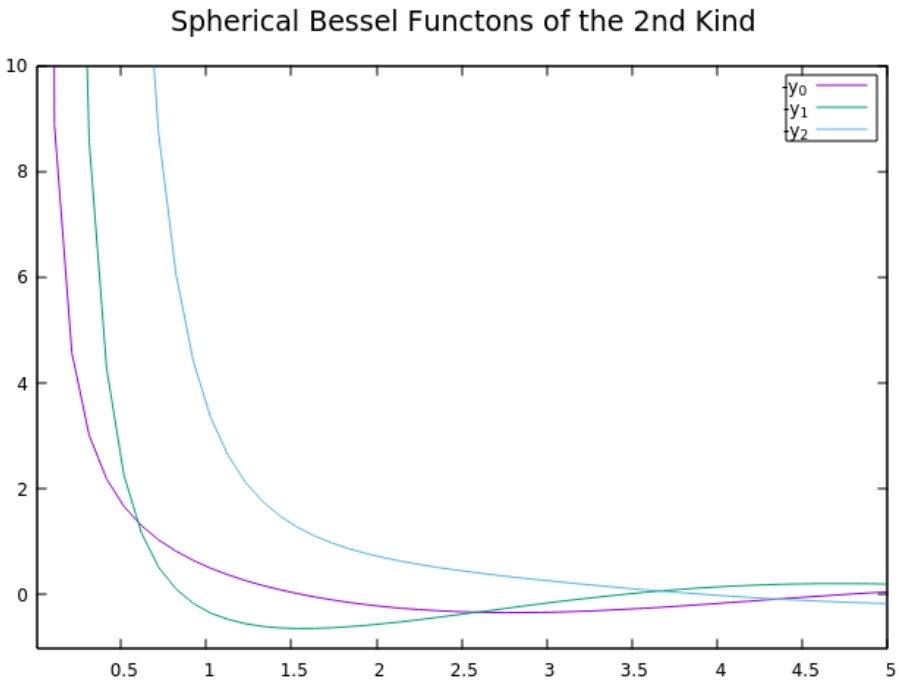

Figure 3.2: Example plot of the first three spherical Bessel functions of the second kind. Superposition of these profiles make up the pressure waves.

In a simulation that uses spherical symmetry, proper care must be placed as to account for wave-driven discontinuities.

3.5 The Counter Flow Diffusion Flame (Combustion)

Given the constraints of spherical symmetry mentioned in the previous section, droplet combustion can be compared to a counter flow diffusion flame with a geometric distortion. The counter flow diffusion flame is a well known scenario[2], so much of the intuition carriers over into droplet combustion.

Given an open environment with two opposing, coaxial, laminar jets, one containing oxidizer and another containing fuel, a stable flame can form. Figure 3.3 shows the bulk flow

[2]Figure 3.3 taken from Moshe Matalon's slide deck on diffusion flames [14]. Equations 3.37, 3.38, and 3.39 are summaries of a few conclusions shown in the slide deck.

of fluid with black arrows and the resultant flame location in red.

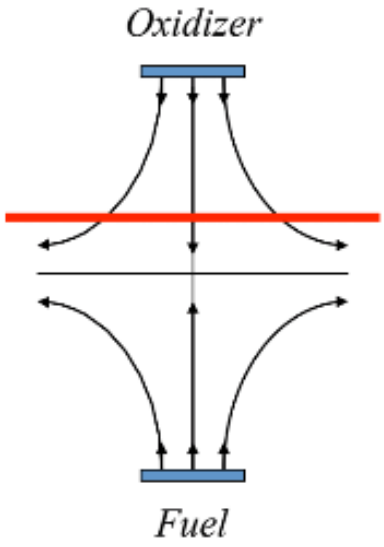

Figure 3.3: Schematic of a counterflow diffusion flame generated by opposing jets.

For infinitely fast chemistry and a unity Lewis number, the concentration and temperature profiles can be derived analytically, as well as the flame stand-off distance. Figure 3.4 shows plots along the concentric axis of the temperature in red, the fuel mass fraction, Y_F, in blue, and the oxidizer mass fraction, Y_O, in green. The flame stand off distance, x_f, is also marked. The profiles follow exponential forms:

$$T = \begin{cases} T_0 + a_1 e^{bx} & \text{for } -\infty < x < x_f \\ T_0 + a_2(1 - e^{bx}) & \text{for } x_f < x < 0 \end{cases} \tag{3.37}$$

$$Y_F = \begin{cases} Y_{F,0} + (1 - a_3 e^{bx}) & \text{for } -\infty < x < x_f \\ 0 & \text{for } x_f < x < 0 \end{cases} \tag{3.38}$$

$$Y_O = \begin{cases} 0 & \text{for } -\infty < x < x_f \\ Y_{O,0} + (a_4 e^{bx} - 1) & \text{for } x_f < x < 0 \end{cases} \tag{3.39}$$

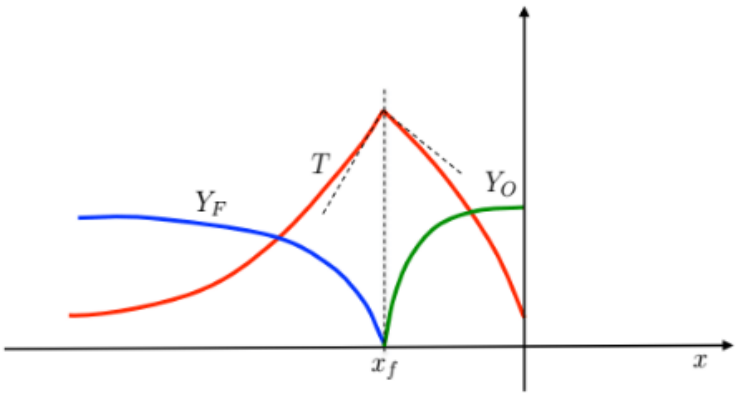

Figure 3.4: Temperature and species profiles or the counterflow diffusion flame.

where, subscript 0 indicates boundary values, a coefficients represent chemistry parameters, and b represents a mass flux term due to the jets.

In the droplet combustion combustion considered here, droplet evaporation can be seen as the oxidizer jet, and the hydrogen diffusion from the environment takes the place of the fuel jet. The exponential-type results of the counterflow diffusion flame should resemble simulation results of droplet combustion, albeit with distortion due to the spherical geometry. This comparison is limited by the time-scale behavior of the two processes. Considering that the jets supply reactants from an infinite reservoir, counterflow diffusion flames represent a steady state process. On the other hand, droplet combustion is inherently transient because of the droplet's finite size. The presence of unsteady terms differentiates the two scenarios.

Chapter 4

NUMERICAL METHODS

The computational methods employed in this researched drew heavily from the open-sourced OpenFOAM project in solving the equations stated in Chapter 2. Modifications were made to the prepackaged combustion solver for ignition applications. Iterative methods were picked due to the stiffness and asymmetries associated with the equations and flow condition. Simulation data was then imported into the Paraview data-visualization program for visual consumption. Lastly, a description of the hardware and logistics used is given.

The methods presented here and the results shown in Chapter 5 were developed in a cyclic process generalized in five steps:

1. Set up numerical method

2. Test and apply method

3. Analyze shortcomings of the test case

4. Modify methods to address problems

5. Repeat at step two until satisfactory

This recursive nature of methods and results leads to an interlinking of dependencies. As such certain parameters and choices in the upcoming chapter may seem arbitrary without context. For a complete description of the physics that the method must resolve, refer to the phenomena presented in the simulation results, as shown in Chapter 5.

4.1 OpenFOAM Environment and Implementation

The OpenFOAM software package offers a suite of partial differential equation solving tools ranging from lagrangian particle dynamics to finite element analysis. Initially coded for analyzing continuum mechanics problems [15], OpenFOAM's main attractions are the dozens of finite-volume solvers. Equipped with a variety of physics capturing abilities, each solver has specific implementation to fluid dynamic simulation. In addition to these solvers, OpenFOAM contains a number of object-oriented structures from which users can create custom solvers. The open source licensing allows users to contribute their codes and increase OpenFOAM's every increasing library of features.

While the prospect of OpenFOAM's free-to-use environment is quite attractive, there are a number of limitations. Using OpenFOAM can be difficult for users unacquainted with non-visual, command-line environments but creating custom tools presents an even harder challenge. The nested structure of inheritance and inter-reliant classes deeply obfuscate the internal solving process. Combined with limited documentation, code manipulation can be compared to navigating a labyrinth. Furthermore the C++ structure of OpenFOAM is well suited for integration with external software and code, but also requires more memory and offers lower speeds than proprietary solvers. Perhaps most important may be the caution needed when analyzing results. The equations used in many solvers may be accurate for a number of validation tests, but this is not a guarantee for all. For example the sonicFoam solver, used for classic CFD problems like the sod-shock-tube [16], was innacurate until version v2.2.0 due to neglect of kinetic energy terms [17]. Therefore users of the OpenFOAM platform should exercise due diligence and check the equations of their solvers to understand the context of results produced.

The reactingFoam model which incorporates multiphase fluid mechanics with chemical interactions serves as the basis for simulate droplet combustion.

4.2 Geometry, Initial Conditions, and Boundary Conditions

Idealize the liquid oxygen emitted by a rocket's injector face as a lone spherical droplet of radius 1mm, surrounded by a hydrogen environment that extends infinitely far away. At a distance of 9mm away from the droplet, the local effects of combustion are assumed negligible and the domain beyond is truncated from consideration. This geometry of the spherical droplet plus surrounding environment exhibits radial symmetry, and so the domain can be reduced to a solid angle slice, approximated by a square pyramid, as shown in Figure 4.1. Overall the computational domain spans 10mm, with a square solid angle of 5 degrees, and an base edge length of approximately 0.872mm.

At the start of simulation the contents of the domain has a continuous temperature of 100K and pressure of 1 bar throughout. The droplet is pre-vaporized and modeled here as a 100% oxygen gas cloud. The ambient environment consists of hydrogen gas diluted with helium. The standard mixture ratio for results contains 1 part H2 for every 3 parts He. Figure 4.2 shows plots of the initial condition, describing temperature, pressure, density and mass fraction.

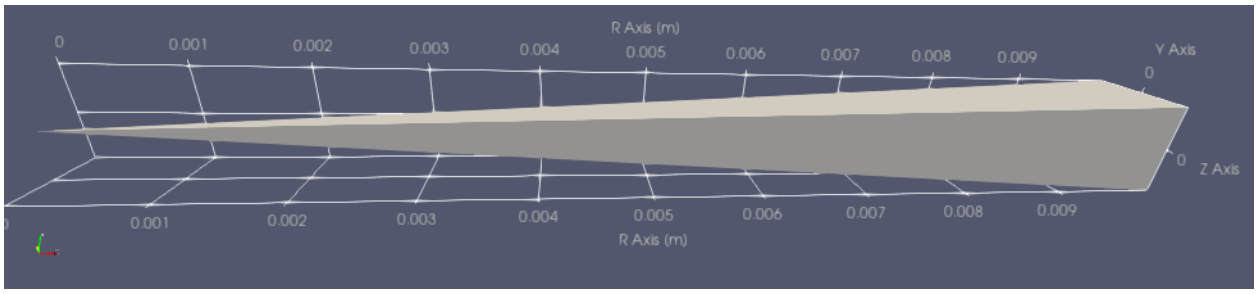

Figure 4.1: Geometry of the computational domain.

The boundary conditions for the domain are quite straightforward. Each of the four radial faces of the pyramid domain represent symmetry boundaries, manifested with OpenFOAM's wedge boundary condition. The tangential face, at the base of the pyramid uses the inlet/ outlet constraint. The boundary allows mass and energy to flow in and out of the

Figure 4.2: Initial conditions

computational domain assuming a fixed exterior pressure, temperature, and composition. As such the prescribed exterior values impose a Dirichlet style constraint on the system and are used similarly to a far field condition.

4.3 Mesh

In the finite-volume method, the geometry is split into a number of smaller cells in which each transport equation is calculated. The pyramidal domain here is segregated into 10,000 cells, such that half reside inside the gas cloud from 0 to 1mm and the rest in the outer environment. The original intention for this choice was to capture higher resolution data near the droplet surface and interior since more cells leads per radial length leads to higher information density. With the number of coupled processes occurring, more data is quite helpful for result analysis.

The computational mesh was constructed in OpenFOAM's blockMesh utility using a linearly increasing cell size. The inner most cell was specified to have a radial length 70 times smaller than the outermost cell. With 10,000 cells on a 10mm length, the aspect ratio of each cell is quite skewed, as seen in Figure 4.3. The average cell length comes out to be

1µm.

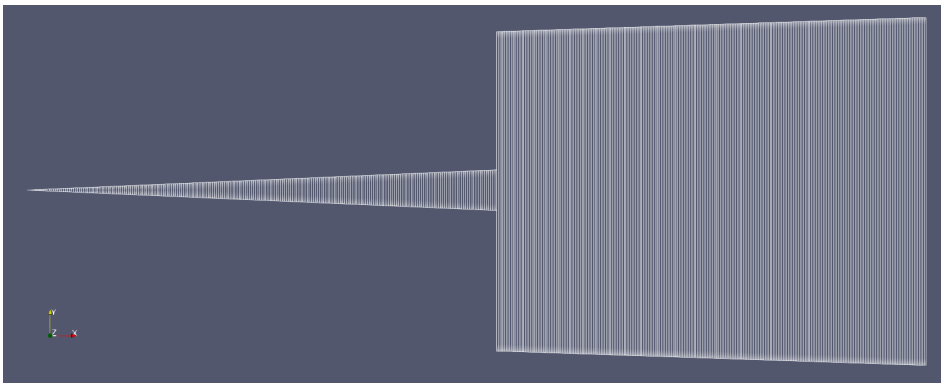

Figure 4.3: Snapshots of the finite-volume mesh. Left image: innermost cells of the spherical radius. Right image: outermost cells of the spherical radius.

4.4 Discretization Schemes

4.4.1 Spatial Advection

Advection occurs through fluxes at the boundary of each cell. In the finite-volume method these fluxes are evaluated at the cell boundaries and summed over the cell through integration. The variable values at cell faces are not known and must be approximated through a Taylor series. The discretization scheme comes into play on how to evaluate the derivatives of the Taylor series expression within the face value interpolation. General discretization of the interpolation scheme uses conditionally 2nd order schemes, a.ka. flux limiters. Except for the momentum advection term, $\vec{\nabla} \cdot (\rho\vec{u} \otimes \vec{u})$, all divergences use the OpenFOAM's implementation of the Sweby limiter[18]. The momentum divergence exception uses a variant of the Sweby Limiter where the fluxes are bound based off the vector component with the highest gradient[1].

[1]Open Foam User Guide 5.0, Section 4.4.3, [12]

4.4.2 Spatial Diffusion

Diffusion processes, usually represented with the Laplacian operator, relies on the gradient operator as well as the divergence operator. Gradients are calculated via the change internal to a mesh cell, which spans across the faces. In these simulations the "Gauss linear" scheme is used where face values are linearly interpolated to neighboring cell centers. This results in a discretization similar to the central differences method found in finite difference method. While Godunov's theorem states this 2nd order discretization is potentially unbounded [19], the additional discretization of the divergence via limited linear divergences negates this problem. The only other gradient term without a divergence operator in the equations noted in Chapter 2 is the pressure differential. This term is overridden through the solver method and is of no direct concern for diffusion. Overall diffusion can be seen to occur from cell center to cell center and is limited mostly by the divergence discretization method.

4.4.3 Temporal

Temporal discretization uses an implicit Euler integration which is equivalent to the finite difference method of backwards Euler discretization. While this method is only first order accurate, it provides stability for the complex coupled equations to be solved.

4.5 ReactingIgnFoam Solver & the PIMPLE Algorithm

OpenFOAM uses a fractional time step method called PIMPLE to solve the conservation laws. The reactingIgnFoam solver uses this method to first solve the species and energy equations and then the mass and momentum equations. Figure 4.4 gives an overview of the algorithm's implementation in reactingIgnFoam. Note that OpenFOAM uses a collocated version, where all data is stored and saved within the cell centers. Face fluxes are established through non-linear interpolation.

Compressible, Collocated PIMPLE Algorithm for reactingIgnFoam, OpenFOAM Implementation:

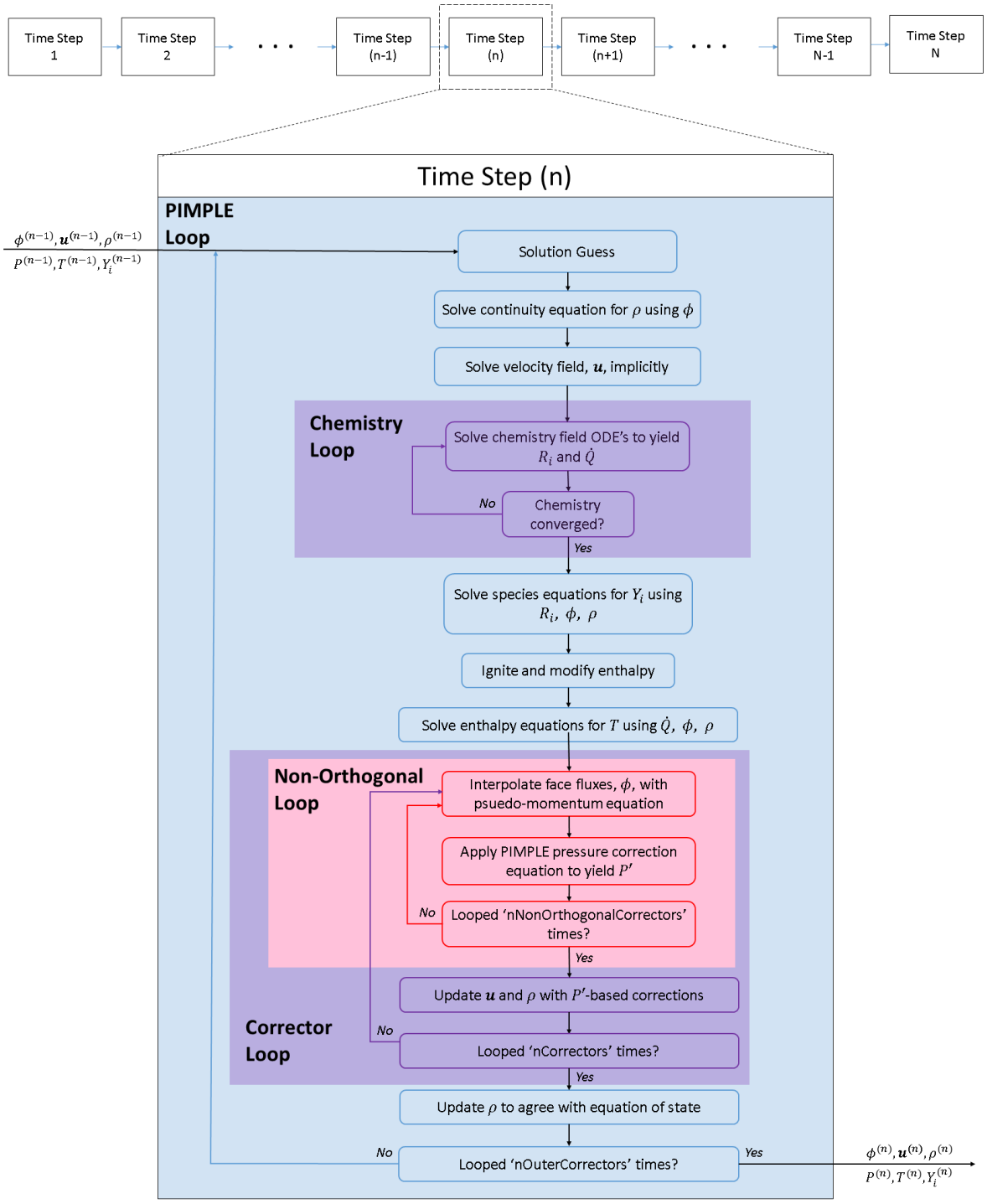

Figure 4.4: Flow chart describing the steps taken within the PIMPLE Algorithm.

4.5.1 Algorithm Steps

4.6 Iterative Methods

4.6.1 Conservation Equations

Each of the equation solving steps mentioned in Section 4.5.1 and in Figure 4.4 represents an equation generally of the form:

$$A\vec{x} - \vec{b} = 0 \tag{4.1}$$

Where the matrix A represents the connectivity and discretization of the mesh, $\vec{b}$ represents internal sources to the cells, and $\vec{x}$ represents cell values. While this equation can be solved directly though matrix inversion, this is not always a feasible option and so a number of iterative methods can be employed based off nature of the A matrix. Some of these methods include preconditioned conjugate gradient (PCG), preconditioned bi-conjugate gradient (PBiCG), and preconditioned bi-conjugate gradient (PBiCGStab) techniques. The preconditioner involved is a computationally less expensive heuristic that reduces the number of total iterations needed to reach convergence. Preconditioners include diagonal incomplete-Cholesky (DIC) and diagonal incomplete-lower-upper (DILU) methods.

Table 4.1 outlines solver settings for single step chemistry and Table 4.2 outlines solver settings for six step chemistry. Note how for six-step chemistry, there are more species involved at lower concentrations, so the residual tolerance is lower than in single step chemistry. The mass continuity equation is missing from these tables because the connectivity matrix associated with the equation is diagonal and needs no inversion or iterative solving.

4.6.2 Chemistry Integration

The system of chemistry ordinary differential equations (ODEs) is quite stiff and is integrated with first order accuracy using OpenFOAM's Rosenbrock integrator. Integration is repeated each of PIMPLE's outer loops and is solved for a relative residual of two orders of magnitude less than initial. One thousand loops is the standard limit for number of loops in which OpenFOAM's ODE solver will attempt to satisfy this residual before triggering a divergence.

Equation	Residual	Units	Iterative Method	Preconditioner
Pressure Corrector	1e-14	Pa	PCG	DIC
Implicit Momentum	1e-11	m/s	PBiCG	DILU
Enthalpy Transport	1e-11	J/m^3	PBiCGStab	DILU
Species Transport	1e-11	-	PBiCGStab	DILU

Table 4.1: Single step chemistry solution settings.

Equation	Residual	Units	Iterative Method	Preconditioner
Pressure Corrector	1e-13	Pa	PCG	DIC
Implicit Momentum	1e-11	m/s	PBiCG	DILU
Enthalpy Transport	1e-12	J/m^3	PBiCGStab	DILU
Species Transport	1e-13	-	PBiCGStab	DILU

Table 4.2: Six step chemistry solution settings.

4.7 Time Stepping & Solver Parameters

The simulation of hydrogen-oxygen combustion was broken down into two main phases: pre-diffusion, and combustion. Before ignition, diffusion acts slowly and predictably. For this reason, time steps were relatively large and residuals coarse. The combustion phase differs however. Due to the presence of ignition waves across the domain, high resolution was required in the form of small time steps and low residual tolerances. Furthermore because of the instantaneous action of diffusion between cells with extreme gradient values, satisfying the CFL condition[20] was not sufficient to ensure convergence.

The combustion phase of simulation can be further broken down into three situations: Standard, Spout, Calm. Standard settings use a constant time step and are the default set up. Spout situations arise when a pressure spike occurs near the origin, causing the standard

settings to diverge. Smaller time steps are used to resolve this effect. The calm situation occurs late in simulation when pressure waves are more tame and gradients have diffused. Table 4.3 outlines the time stepping parameters.

Simulation Phase	Time Step Size (s)	Start Time (s)	End Time (s)
Diffusion	1e-06	0.0000	0.0150
Standard Combustion	1e-10	0.0150	0.0162
Pressure Spike	1e-11	As Needed	-
Calm Combustion	1e-09	0.0162	0.0183

Table 4.3: Time stepping schemes and the time step marker for single step chemistry.

4.8 Paraview Post-Processing

The simulation data was loaded into Paraview, the open-source data analysis and visualization application, for post processing. Paraview comes with a number of highly customizable features and offers a well documented user manual [21].

The basic template for data presentation was generated in Paraview and consists of four diagrams, all with an x-axis representing radial distance in units of meters:

1. Time stamp (in units of seconds) and geometry colored with temperature

2. Chart of species mass fraction (left axis) and temperature in units of K (right axis).

3. Chart of pressure in units of *bar* and density in $\frac{kg}{m^3}$ (left axis) with signed Mach number (right axis).

4. Chart of volumetric heat generated by chemical reaction in units of $\frac{W}{m^3}$ and plotted on a log axis.

This standard figure used to show results, while complicated, gives a great overview of simulation status. Composition, state properties, bulk transport, and chemistry are all represented. Figure 4.5 shows the standard figure for the initial conditions.

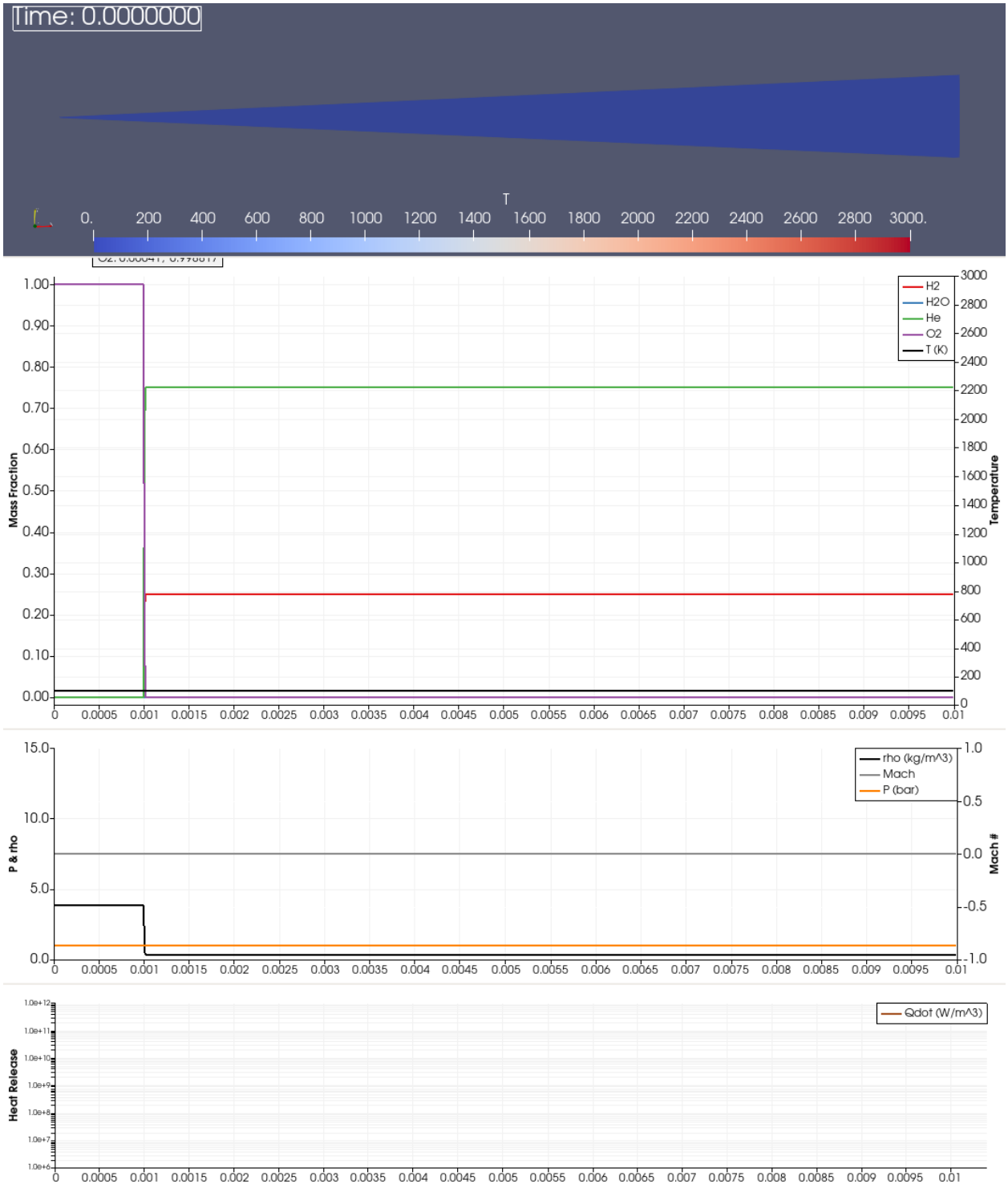

Figure 4.5: The standard Paraview plot for presenting results. Initial conditions are shown.

The six-step chemistry model uses a modified version of the heat release diagram due to the presence of endothermic reactions (particularly the disassociation of hydrogen from diatomic to mono-atomic). The relative strength of reaction is still visible from the log axis but the problem of negative values is avoided by splitting heat release data into two domains via a sign filter. Paraview does not support the 'sign()' function natively and so the procedure follows:

$$|\dot{Q}_{Exothermic}| = \mathcal{H}\big(\text{sign}(\dot{Q})\big) \cdot \dot{Q} \tag{4.2}$$

$$\approx \left[\frac{\arctan(\dot{Q})}{\pi} + \frac{1}{2}\right] \cdot \dot{Q} \tag{4.3}$$

$$|\dot{Q}_{Endoothermic}| = \mathcal{H}\big(\text{sign}(-\dot{Q})\big) \cdot -\dot{Q} \tag{4.4}$$

$$\approx \left[\frac{\arctan(-\dot{Q})}{\pi} + \frac{1}{2}\right] \cdot -\dot{Q} \tag{4.5}$$

Figure 4.6 shows an example of the filtered heat release data using Equations 4.3 & 4.5.

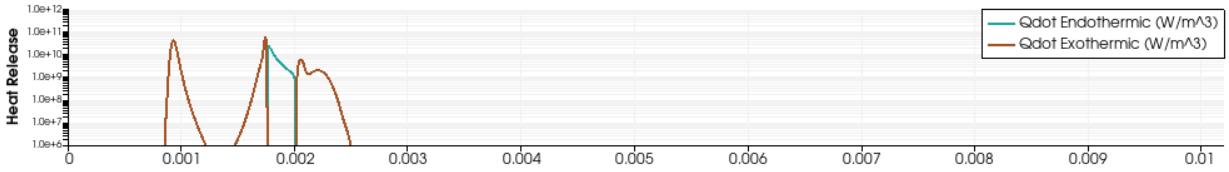

Figure 4.6: The modified heat release plot for presenting results in six step chemistry simulation. An arbitrary, example time step is shown.

Additionally the six-step chemistry presents the minor species, O, H, and OH, on a separate plot of mass fraction. Due to the large variations in these minor specie concentrations, trends are displayed on a semi-log axis, as seen in Figure 4.7.

4.9 Hardware

Simulations were carried out in steps due to long run times of multiple weeks. Often times OpenFOAM was run in parallel on the University of Washington Aeronautics and Astronautics (UWAA) computer cluster, Cerberus. Cerberus contains twenty nodes of either 24

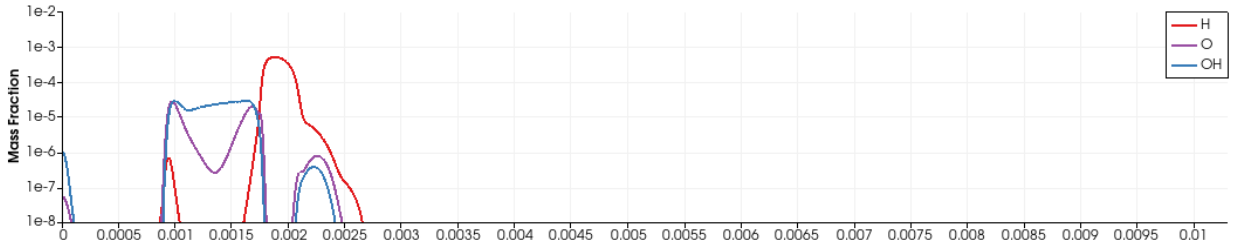

Figure 4.7: Plot of minor species on a semi-log axis exclusive to presentation of six-step chemistry results.

(Intel Xeon E5-2620) or 40 processors (Intel Xeon E5-2660), of which 15 are available for student access. Simulations ran on Cerberus at anywhere between 96 to 160 processors. Note that the Cerberus processors used hyperthreading to expand potential data messaging efficiency, OpenFOAM is unable to take advantage of this as of version 5.x. As such while 160 processors may have been occupied, only 80 physical cores were in use. First runs of most cases as well as the tackling of certain divergence walls were typically resolved on the author's laptop using 4 physical processors (Intel i7-3632Q).

Animations processed in Paraview, were typically carried out on the UWAA remote server, RDSH-2. RDSH2 provides faux-desktops of any resolution requested and as such was great for Paraview, which can only render images as large as the current display. The faux-desktop resolution was set to 3000x2000 pixels which allowed for painless downscaling to 1080p resolutions (1920x1080).

Chapter 5
RESULTS

The two main simulations of one and six step chemistry share the same results for the first stage of simulation, pre-diffusion. After this stage the results of the two simulations diverge not just in composition but in temperature distribution as well. While simulations are comparable in some respects and share many of the same behaviors, the differences are noticeable.

5.1 Pure Diffusion

The diffusion profile after 15 ms of simulated time can be seen in Figure 5.1 on page 38. Note how the diffusion profiles resemble elongated error functions in shape.

5.2 Combustion with Single Step Chemistry

The single-step chemistry simulation ran for a 3.2 milliseconds post ignition for a total simulation time of 0.0182 seconds. Due to prolonged run time (on the order of weeks), total computation time was not tracked. The state of simulation results can be categorized post-diffusion into the following scenarios: applied ignition, spontaneous combustion, flame formation, pseudo-steady combustion, and droplet extinction.

5.2.1 Ignition

The input ignition was mild, only producing a spark temperature of 298 K. Figure 5.2 shows the applied spark. Note the the contact discontinuities in momentum, pressure, and density. Ignition does not result in sustained reaction until multiple sparks have been introduced. At time 0.0150031 s, combustion occurs violently producing a peak temperature of 6340 K.

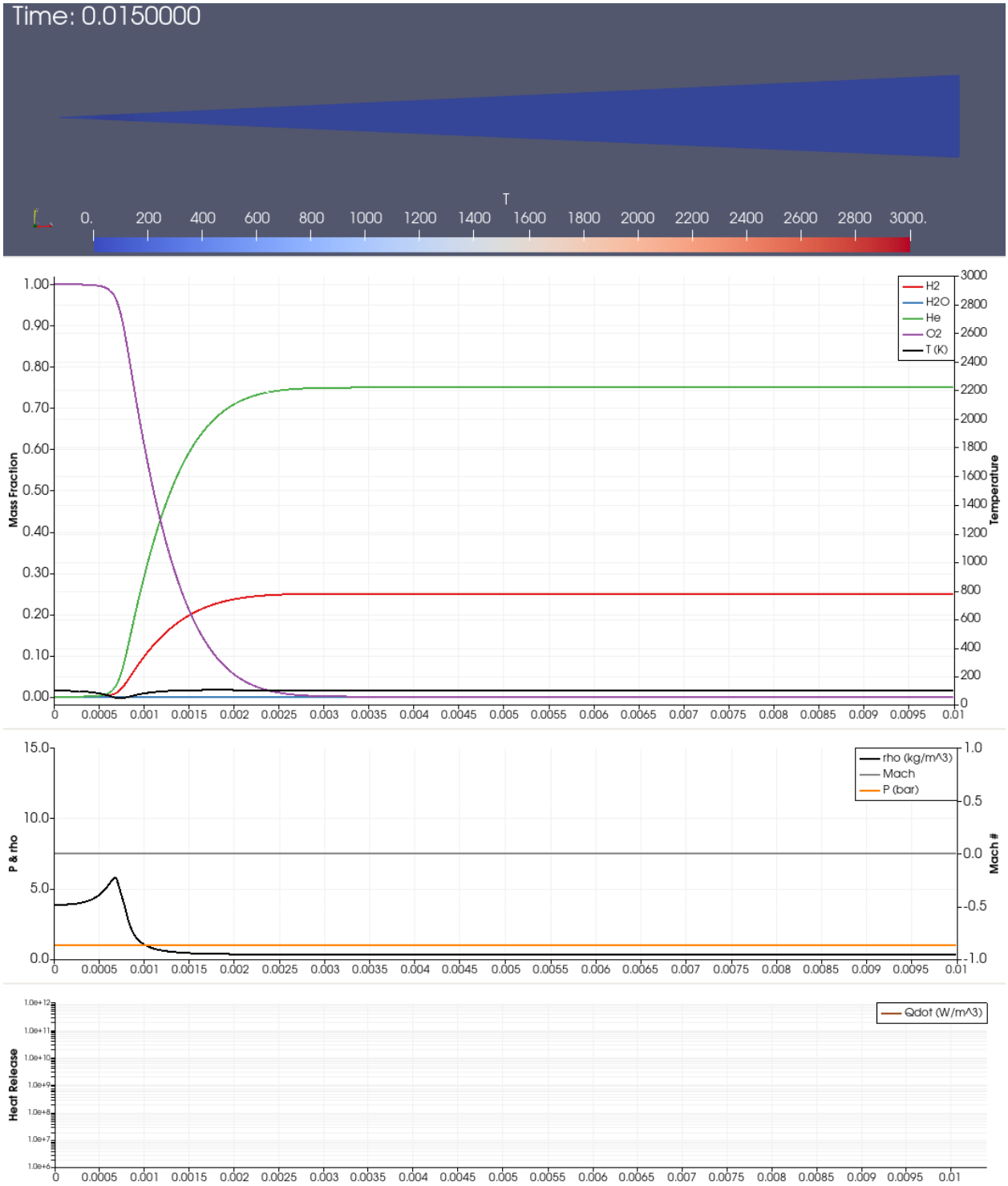

Figure 5.1: Diffusion carried out for a total of 15ms.

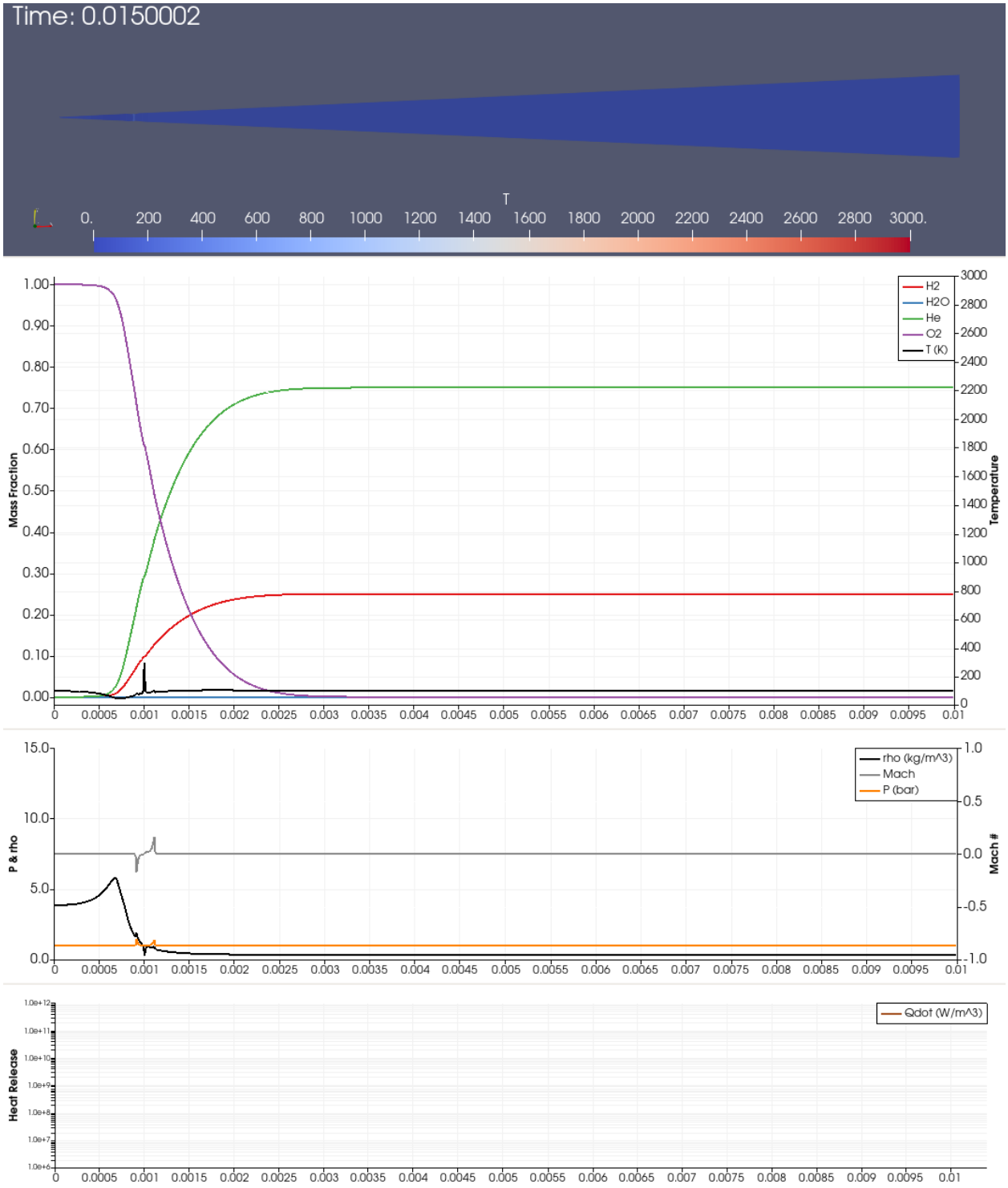

Figure 5.2: Single step chemistry after a few ignition attempts.

5.2.2 Flame Formation

Flames formation occurred after ignition in six steps:

1. Spontaneous detonation formed combustion products on site of ignition application forming a barrier between two distinct pre-mixed regions of fuel and oxidizer. Event time stamped at 0.0150031 seconds in Figure 5.3 on page 42.

2. The ignition reaction travels both inwardly and outwardly due to the thermal expansion of the combustion products. Two flame zones are apparent through heat release locations. The local temperature does not reflect the flame location suggesting a non-equilibrium state. See Figure 5.4 on page 43.

3. The local depletion of oxidizer in the newly formed hot region between the two flames causes a large species concentration gradient. The large diffusive flux of oxidizer from the oxygen gas cloud halts the inwards traveling flame zone, setting it in place barely inwards of the ignition application site. The outwards-traveling wave continues moving. See Figure 5.5 on page 44.

4. The pressure wave resulting from the initial combustion bounces off the droplet center and hits the inner reaction zone. At this point the entire locality of the gas cloud and ignition region has a bulk flow outwards, bringing oxidizer into the hot region faster than the inner flame can consume. This causes the inner premixed flame to spit out a diffusion flame that consumes the leftover fuel in the hot region as well as the bulk transported oxidizer. See Figure 5.6 on page 45.

5. The central diffusion flame stabilizes at the same time as the outwards traveling pre-mixed flame. This coincides with a relative stop in bulk flow motion, most likely because the compositional barrier formed by oxygen and combustion products reflects most momentum fluxes. The apparent three flames have stabilized in relative position. See Figure 5.7 on page 46.

6. The temperature profile diffusively conforms to the hot region, forming a peak at the location of the central diffusion flame. This quasi-equilibrium occurs at a time of 0.0150600 seconds, 56.9 μs after spontaneous detonation. See Figure 5.8 on page 47.

Further wave reflection, propagation, and emission continue to perturb the overall combustion structure but do not affect the relative temperature profile/ flame location coupling. No new waves are generated, the reflections linger within the domain. This state places combustion in pseudo-steady-state where the overall process is transient but stable structures are formed.

5.2.3 Pseudo-Steady Combustion

The pseudo-steady combustion phase is characterized by the relatively larger time scale of occurrence, compared to flame formation. The two premixed flames are slowly consumed during this time span with their reaction profiles diminishing and widening as well. Furthermore as combustion produces heat, the hot region expands as well. See Figures 5.9 (page 48) and 5.10 (page 49) for examples of this process.

Throughout this phase, and even seen during flame formation, are burst of combustion and heat release near the center of the oxygen gas cloud, usually coinciding with a pressure spike occurring at the origin. Figure 5.11 on page 50 shows an example of the combusting pressure spike.

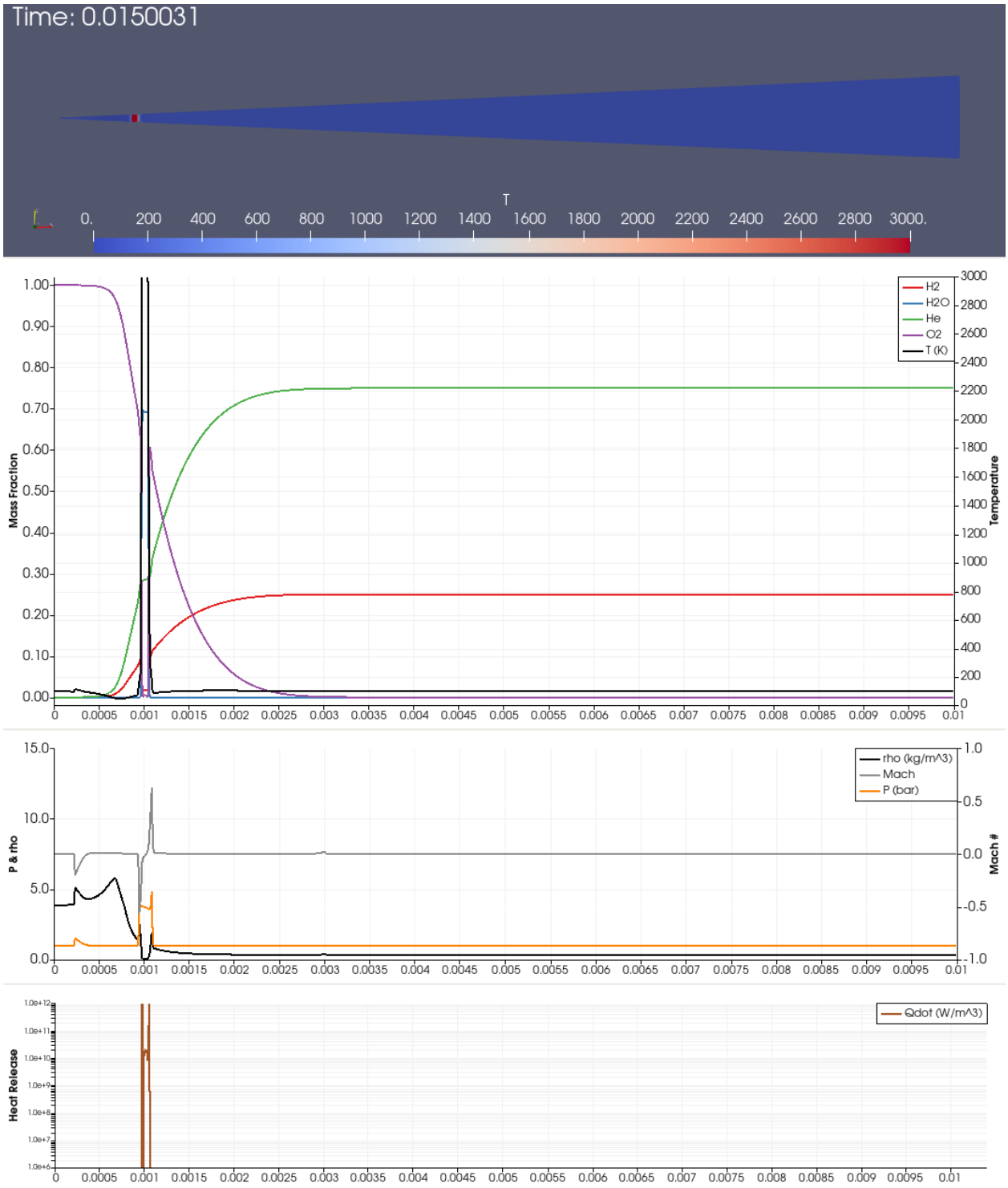

Figure 5.3: Single-step chemistry: Combustion occurs violently after many ignition attempts.

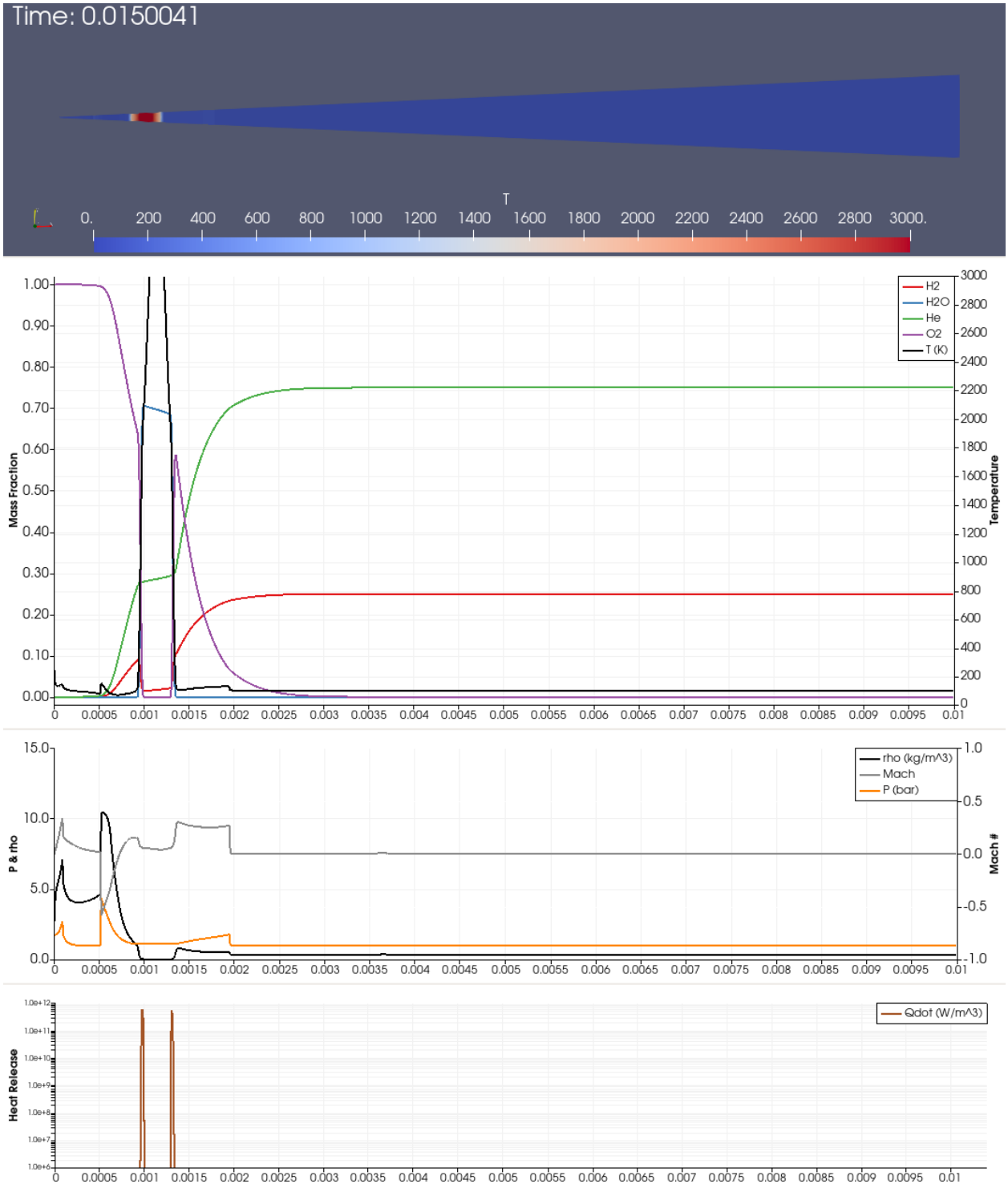

Figure 5.4: Single-step chemistry: Detonation waves travel both directions, away from ignition point.

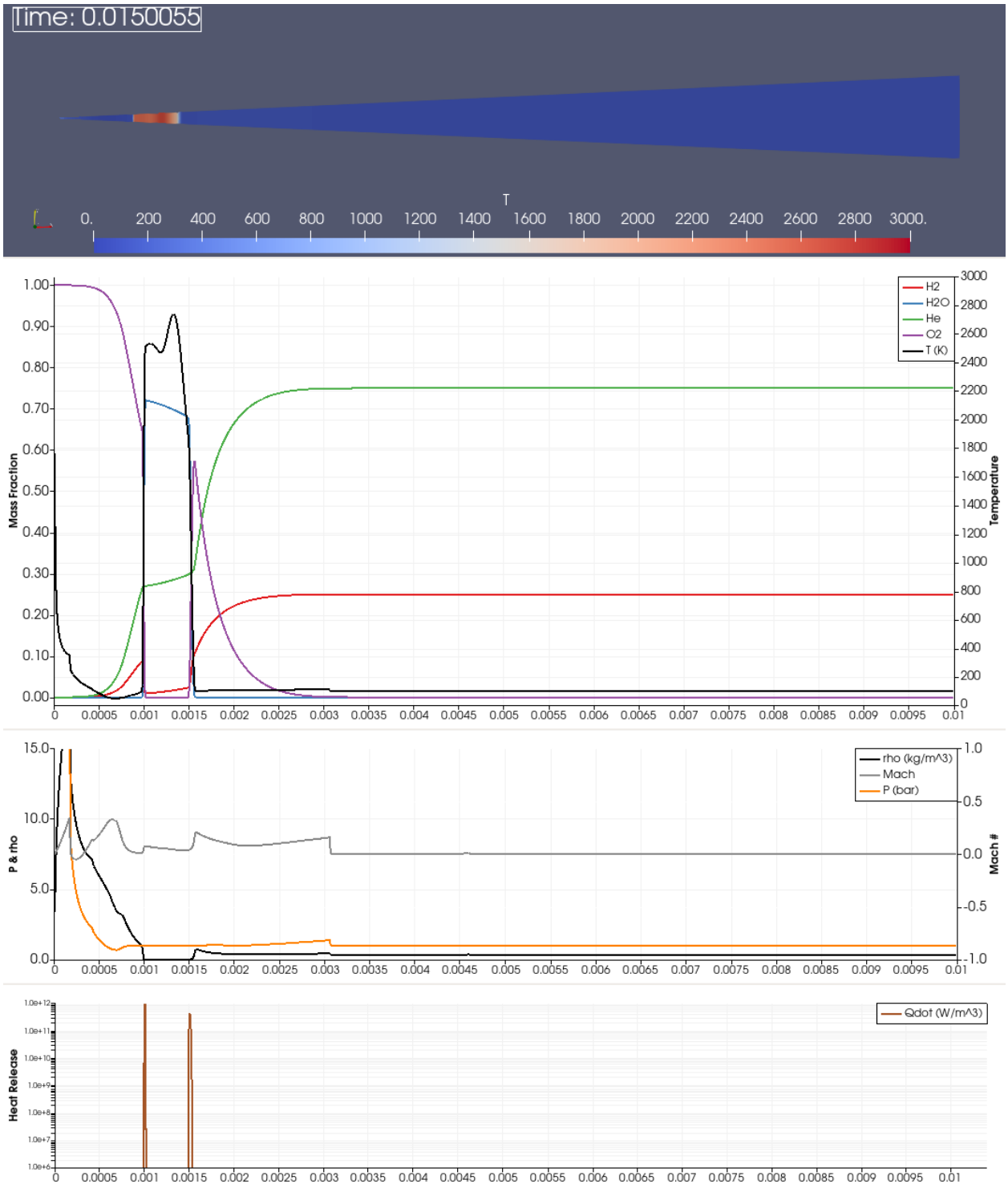

Figure 5.5: Single-step chemistry: Inner flame becomes stationary due to increased diffusion.

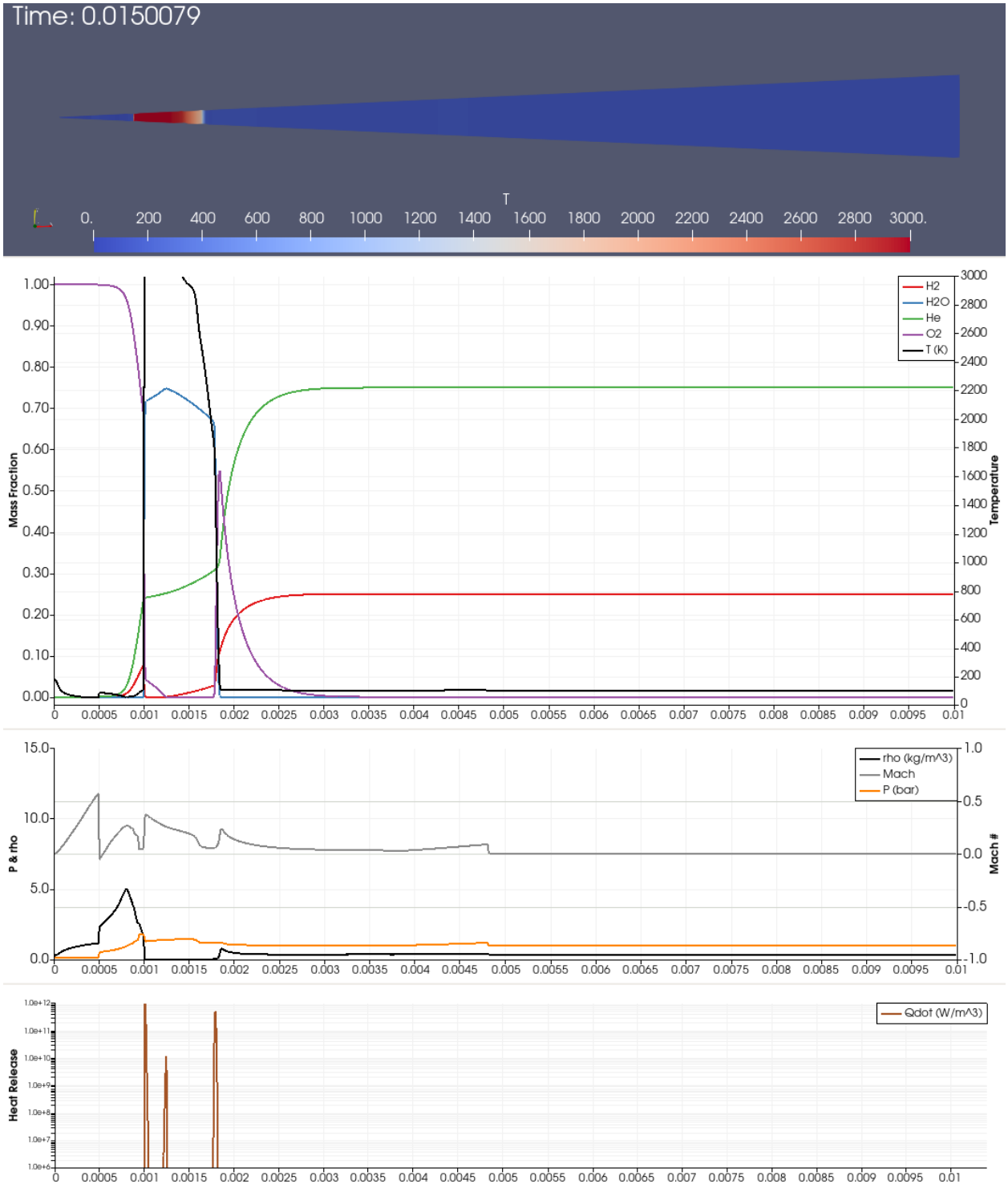

Figure 5.6: Single-step chemistry: A diffusion flame is formed upon impacted of reflected detonation wave.

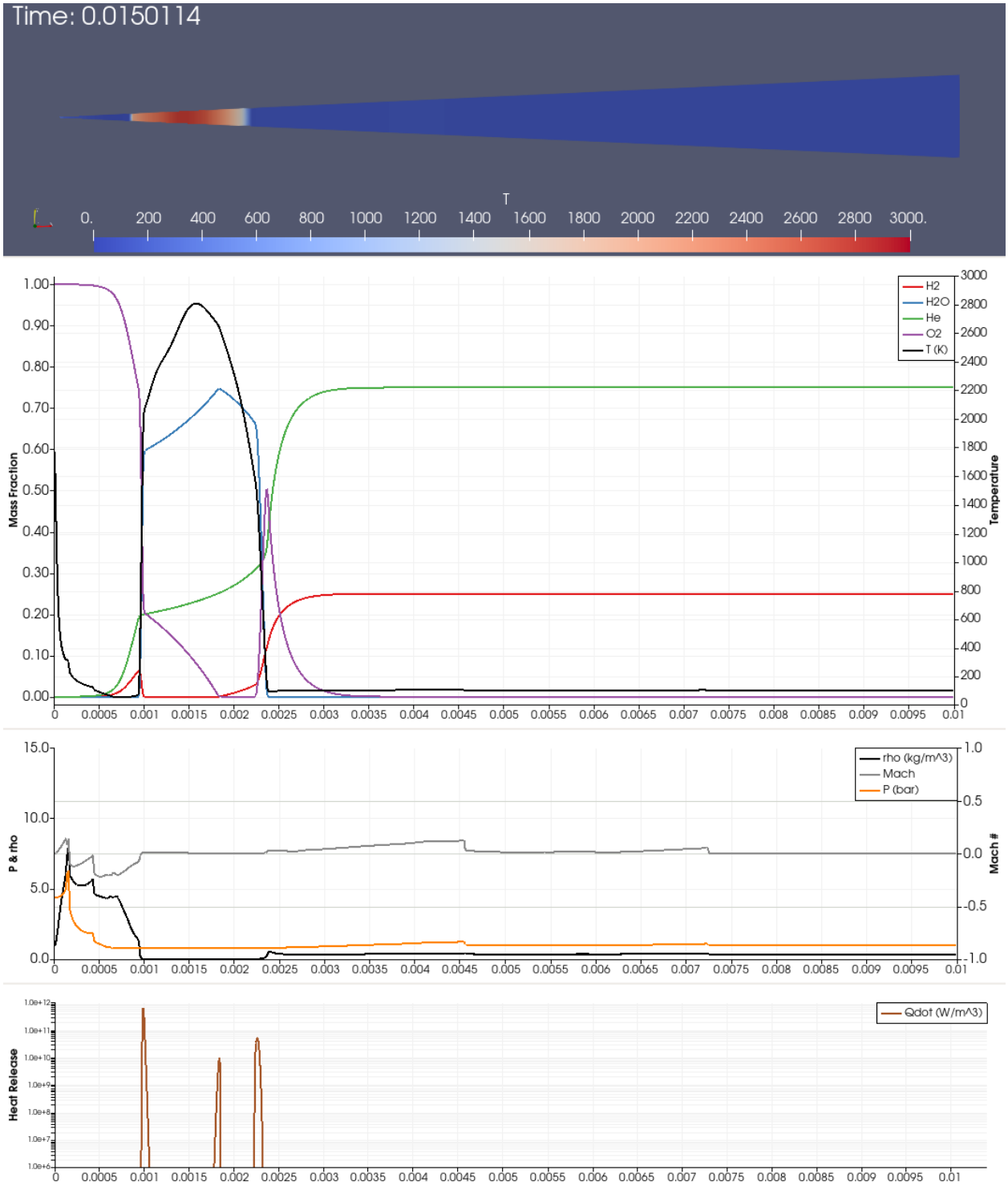

Figure 5.7: Single-step chemistry: Stabilization of flame formation. Two premixed flames are situated on either side of a diffusion flame.

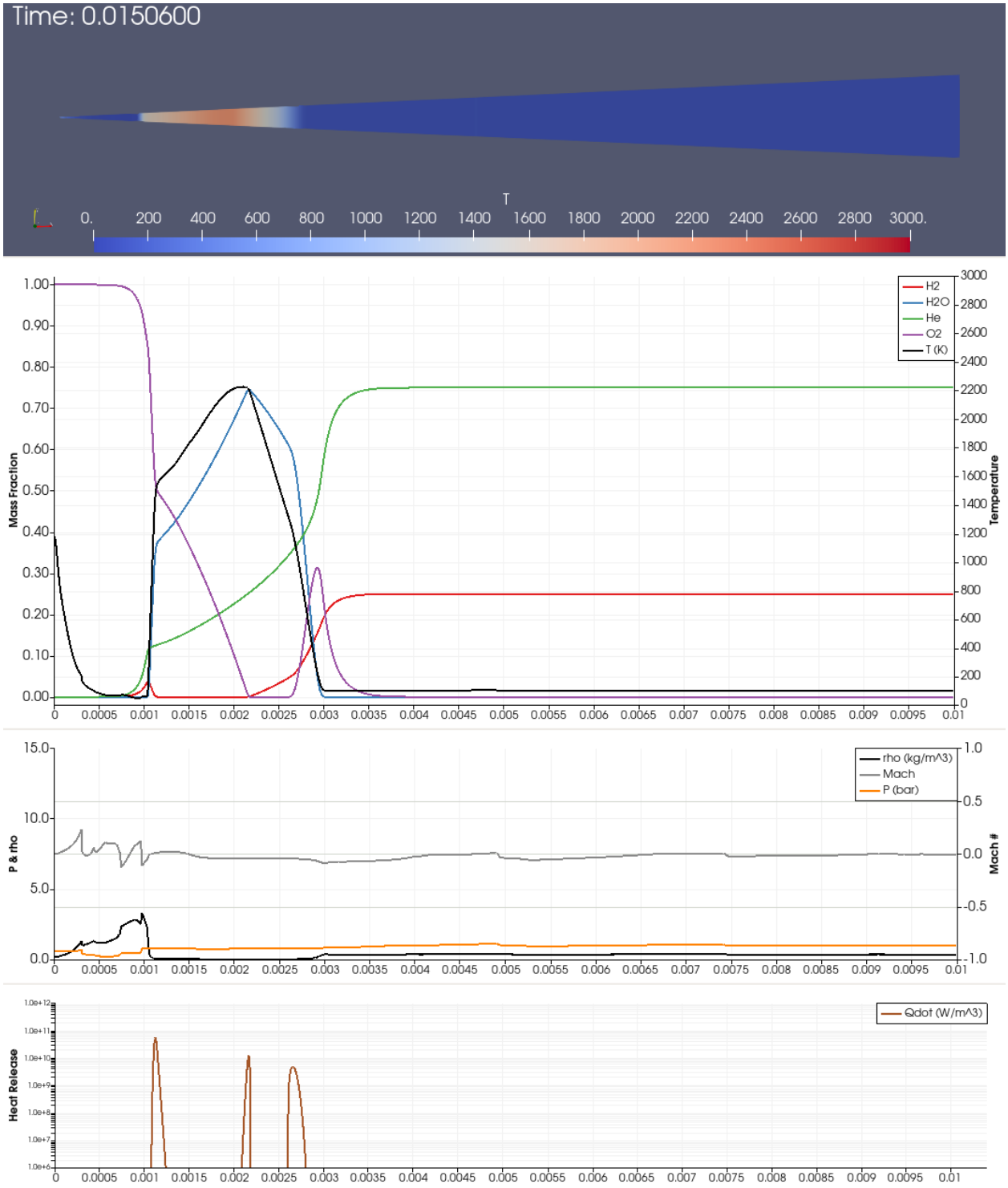

Figure 5.8: Single-step chemistry: The peak temperature location matches the diffusion flame placement leading combustion in to pseudo-steady-state behavior.

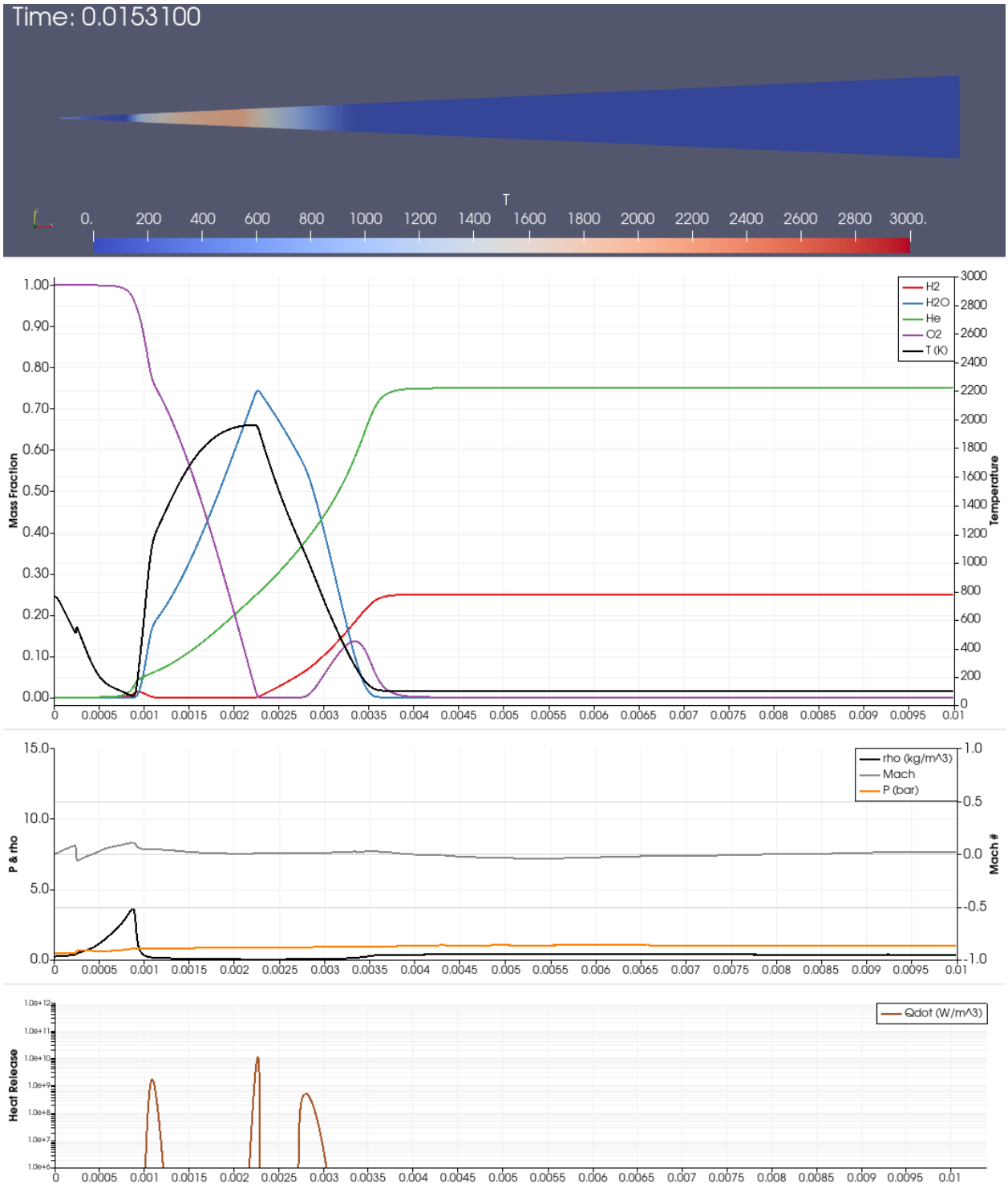

Figure 5.9: Single-step chemistry: Progression of pseudo-steady combustion - example 1.

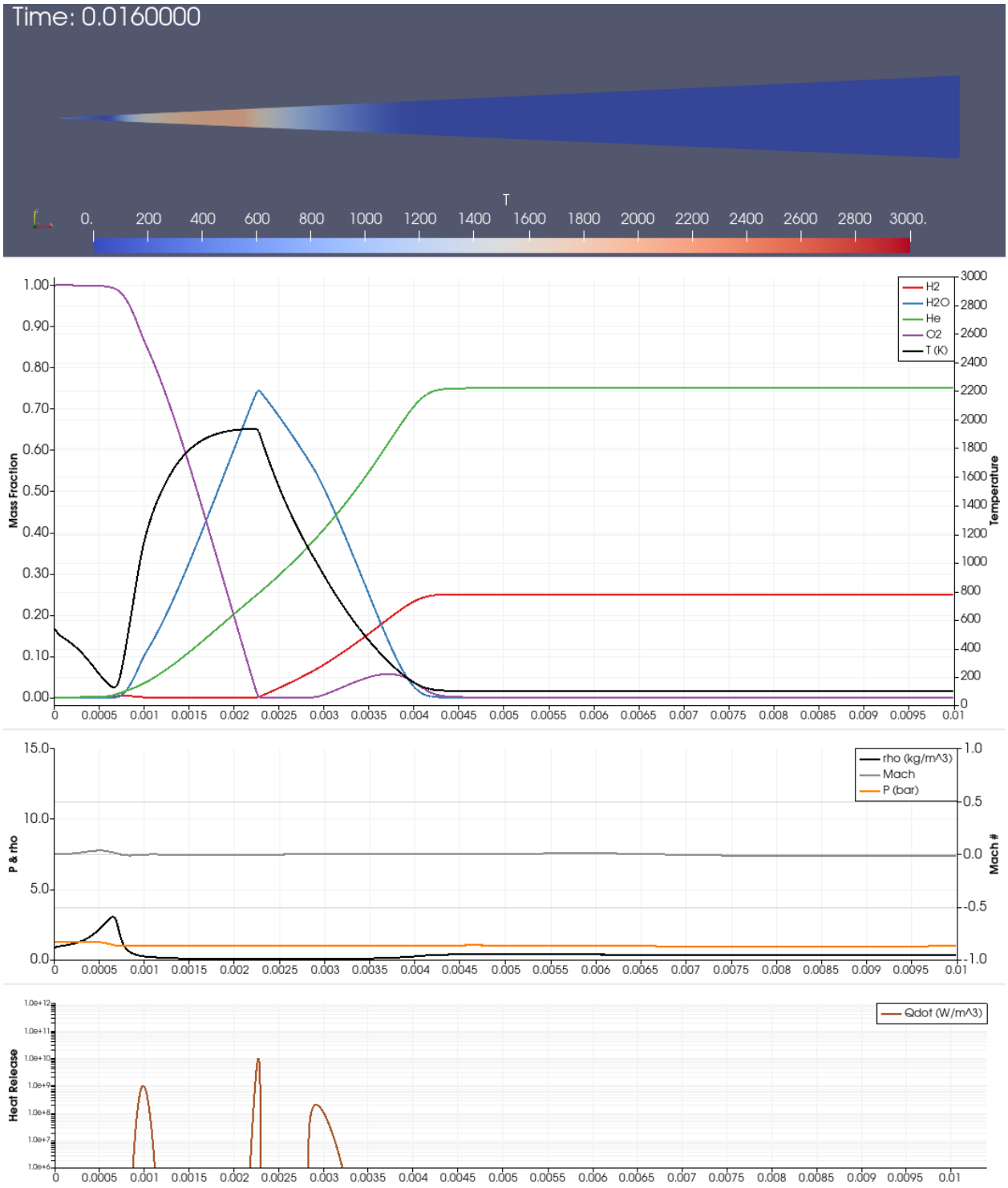

Figure 5.10: Single-step chemistry: Progression of pseudo-steady combustion - example 2.

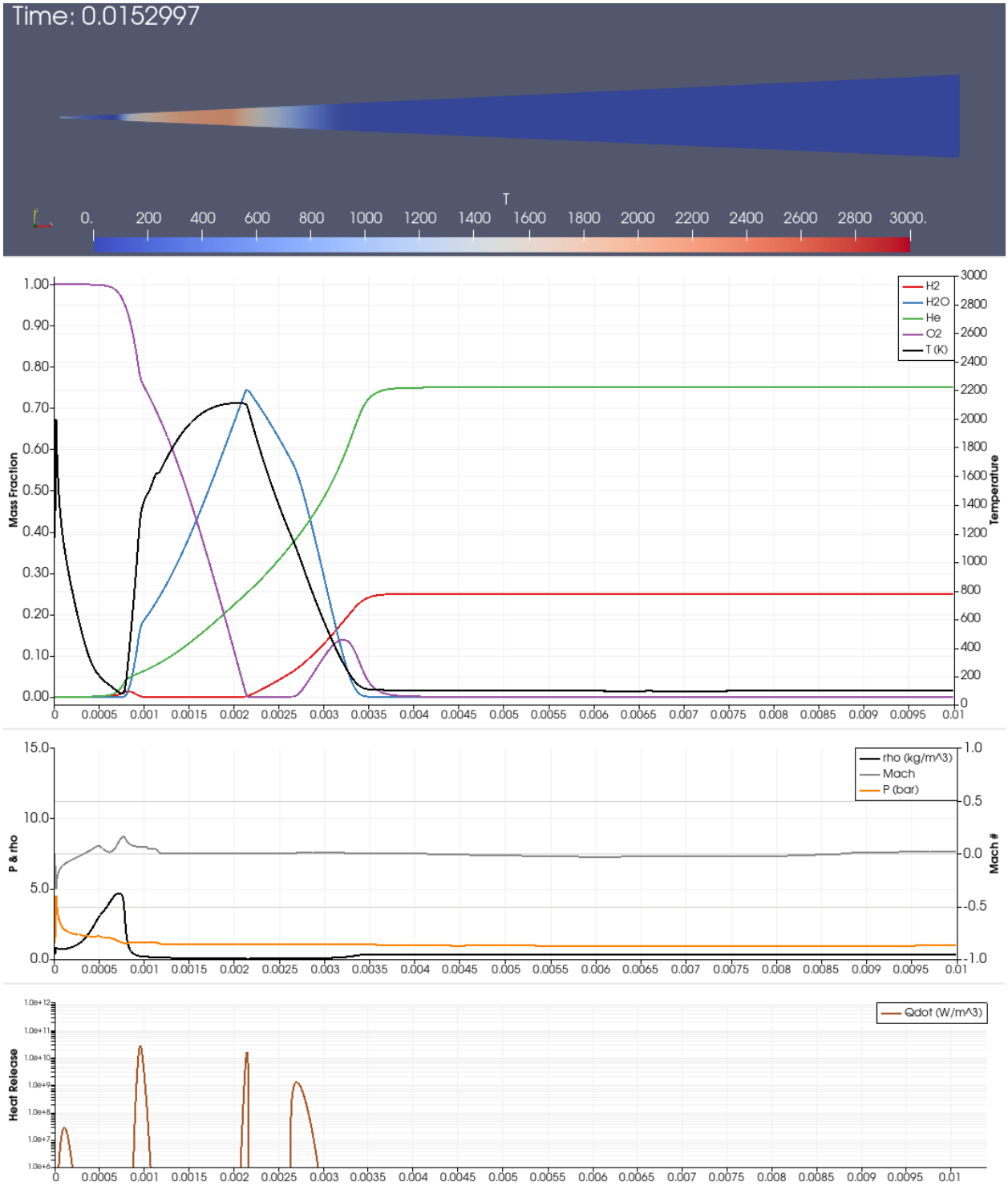

Figure 5.11: Single-step chemistry: Combustion occurs within the pre-vaporized oxygen droplet on select occurrences of pressure spikes.

5.2.4 Droplet Extinction

Droplet extinction is the stage of combustion in which the reservoir of oxygen gas (the droplet) shows significant depletion and combustion shows signs of deceleration. Figure 5.12 shows time 0.018262, one of the last time steps calculated in the single-step chemistry simulation. No location in the domain at this point is fully oxygen gas. the center of the domain presents the oxygen composition maximum at ≈90.9%. With the interior of the domain heated to roughly the flame temperature, ≈2000 K, and the centroid of droplet mass at ≈1mm, less than 5% of the initial oxygen mass is present in the domain. The inner premixed flame is not longer present due to complete hydrogen consumption in the local region. This extinction event occurs at a times of 3.231 ms after the start of combustion.

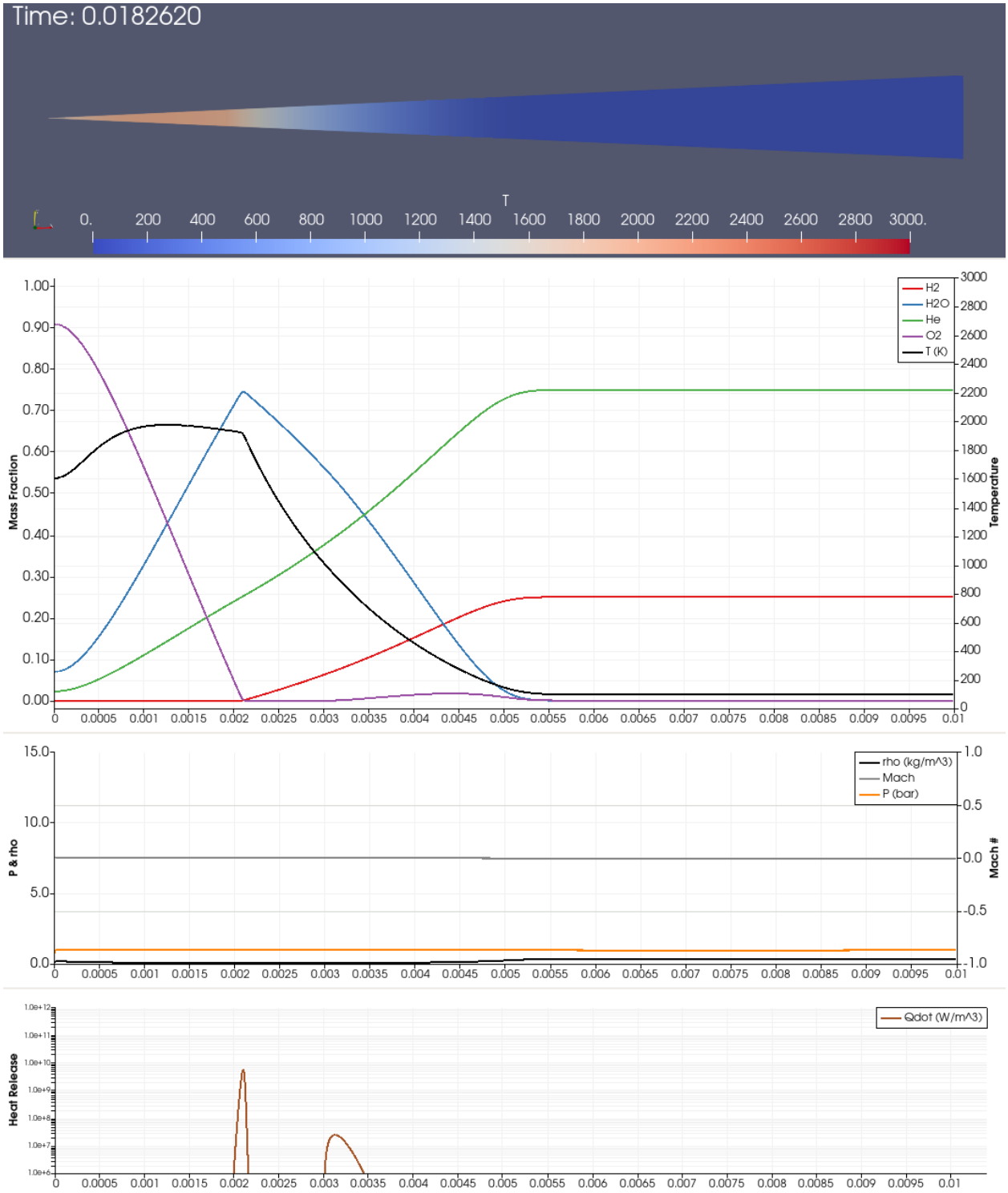

Figure 5.12: Single-step chemistry: The droplet being near total consumption and the deceleration of combustion marks the beginning of droplet extinction.

5.3 Combustion with Six Step Chemistry

The six-step chemistry simulation ran for a 0.4 milliseconds post-ignition for a total simulation time of 0.0154 seconds. The computational time was not tracked here though its worth noting that the runtime per time step for six-step chemistry was at least twice as long than a single-step chemistry timestep. The states of simulation results can be categorized post-diffusion into the following scenarios: ignition & initial combustion, flame formation, and pseudo-steady combustion. Droplet extinction was not simulated due to the excessive computation times required. The first 1e-9 seconds of the simulation were run using time steps of 1e-11 seconds due to divergence issues with the solver.

5.3.1 Ignition & Initial Combustion

The same ignition parameters used in the single-step chemistry immediately ignited the mixture under the six-step chemistry model. Figure 5.13 on page 56 shows the resulting explosion from ignition. Contact discontinuities in momentum, pressure, and density are present once again. Initial combustion temperature was similar to the single-step model with peak temperature of 6794 K. While the peak temperature of single-step combustion exceeded 5000 K on the order of 1e-8 s, the peak temperature of the six-step simulation decreased to ≈4000K in 4e-11 seconds. After time on the order of 1e-8 seconds, temperatures reduced to ≈2500K making this a relatively tame ignition event.

5.3.2 Flame Formation

Flame formation occurred after ignition in five steps, similar to the first five steps of the single-step simulation:

1. Spontaneous detonation formed combustion products on site of ignition application forming a barrier between two distinct pre-mixed regions of fuel and oxidizer. See the

event time stamped at 0.0150000 seconds in Figure 5.13 on page 56.

2. The ignition reaction travels both inwardly and outwardly due to the thermal expansion of the combustion products. Two flame zones are apparent through heat release locations. An endothermic region exists between the two flame zones, marking a region of hydrogen radical formation. The local temperature does quite not reflect the flame location but the endothermic region does correlate with a temperature dip in the same location. This somewhat matched heat release and temperature profile suggests a partial equilibrium. See Figure 5.14 on page 57.

3. The local depletion of oxidizer in the newly formed hot region between the two flames causes a large species concentration gradient. The large diffusive flux of oxidizer from the oxygen gas cloud halts the inwards traveling flame zone, setting it in place barely inwards of the ignition application site. The outwards traveling wave continues moving. See Figure 5.15 on page 58.

4. The amount of oxygen radical on the inner flame reaches a maximum at a mass fraction value of 7.6e-4. This correlates with the splitting of the inner flame region, with the newly formed exothermic zone being a diffusion. Perhaps the diffusion flame is formed because of the excess oxidizer radicals (O and OH) building up in the inner flame, and spilling out into the hot region where species are more mobile. Note that the formation occurs later than the single-step simulation, since the initial detonation wave reflection has already occurred. Furthermore the peak temperature follows the diffusion flame location tightly throughout the formation process. See Figure 5.16 on page 59 for a snapshot immediately before the diffusion flame forms and Figure 5.17 on page 60 for after.

5. The central diffusion flame stabilizes at the same time as the outwards traveling premixed flame. This coincides with a local halting of bulk fluid motion, most likely

because the compositional barrier formed by oxygen and combustion products reflects most momentum fluxes. The three flames appear to have reached stable positions. The temperature profiles have also conformed to the reaction zones as much as they will throughout simulation. This brings combustion into quasi-equilibrium at a time of 0.0150281 seconds, 28.1 μs after spontaneous detonation. See Figure 5.18 on page 61.

Further wave reflection, propagation, and emission continue to perturb the overall combustion structure but do not affect the relative temperature profile/ flame location coupling. This state places combustion in pseudo-steady-state where the overall process is transient but stable structures are formed.

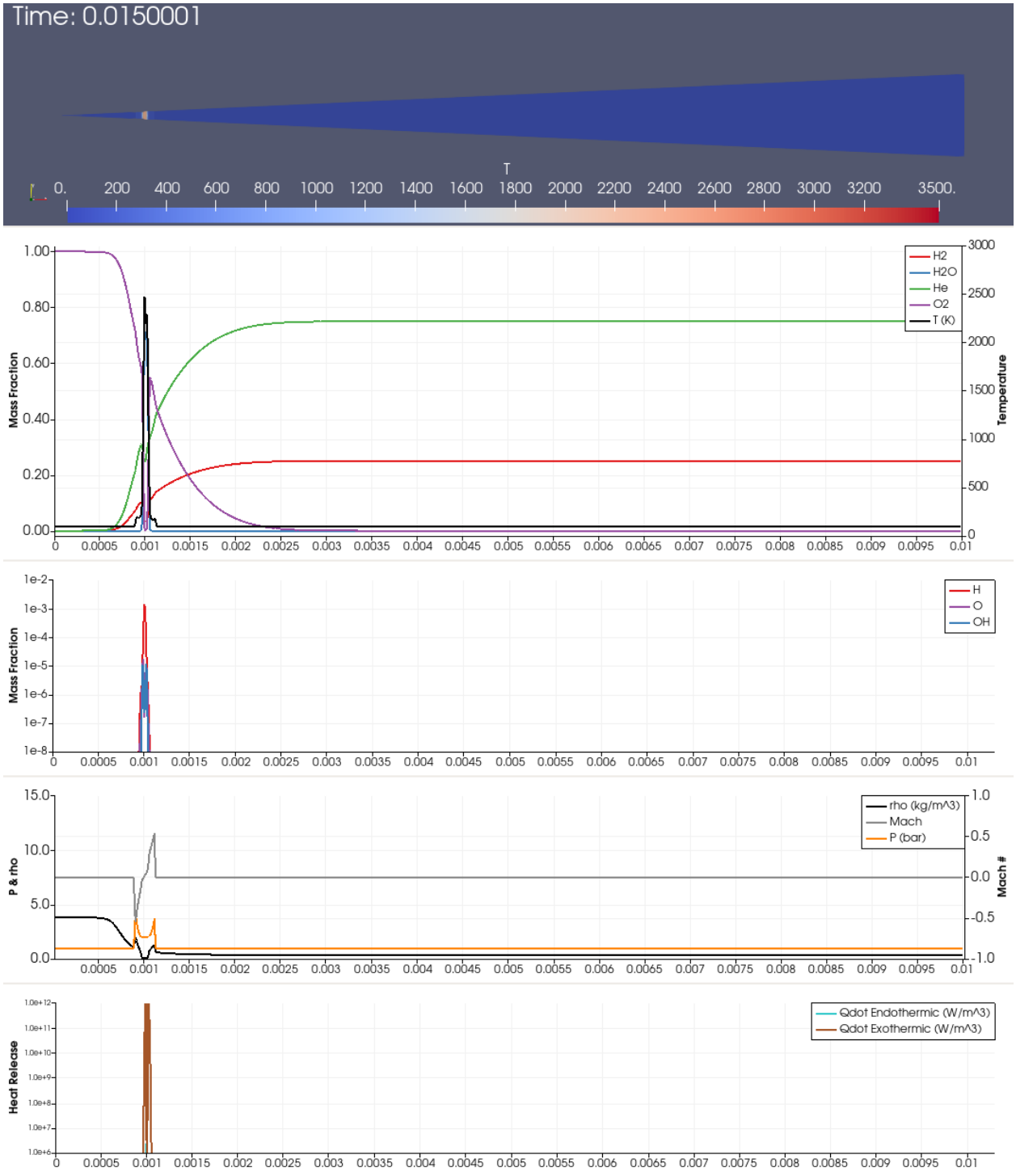

Figure 5.13: Six-step chemistry: Combustion occurs upon the first ignition attempt. No subsequent sparks are introduced.

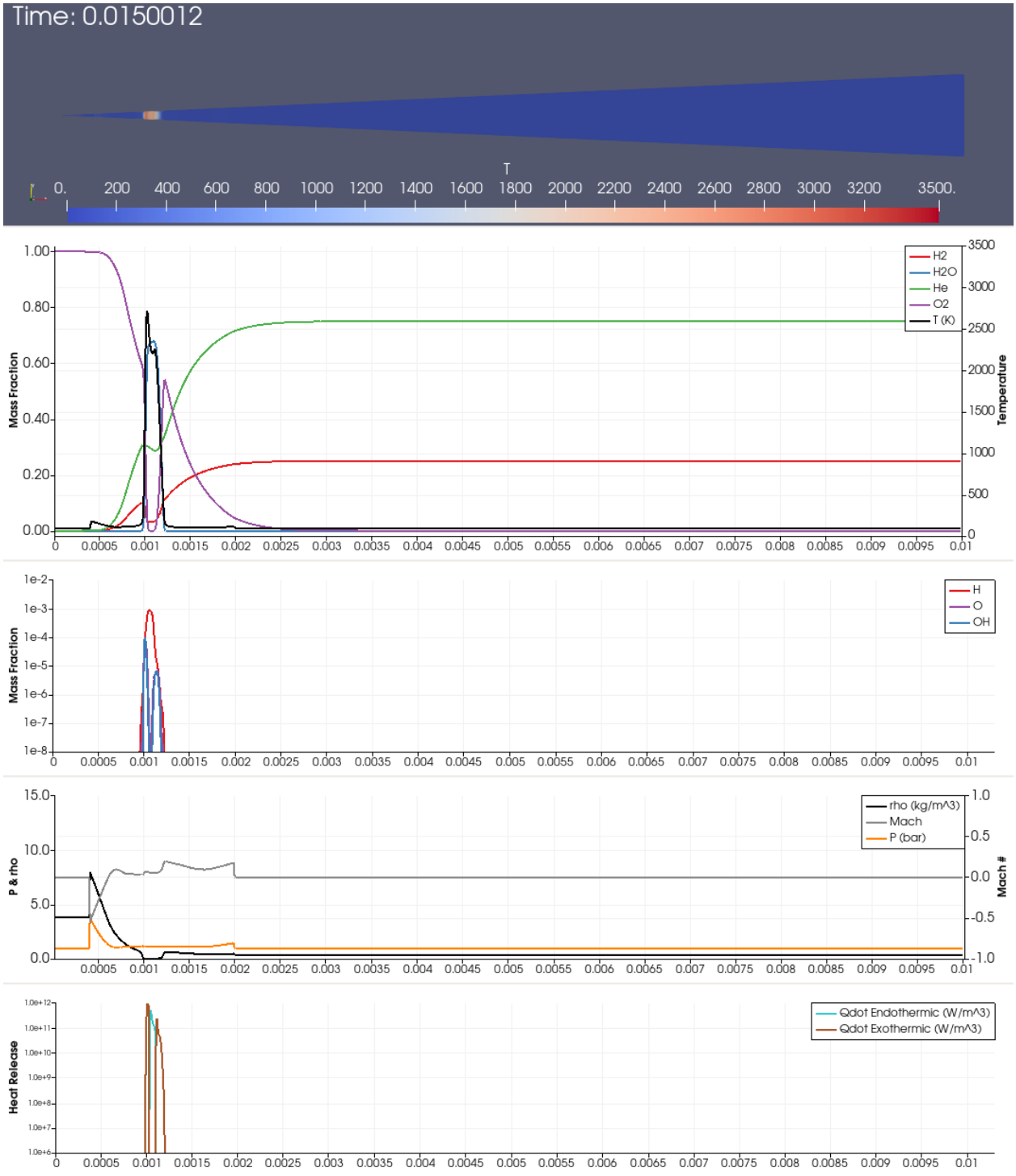

Figure 5.14: Six-step chemistry: Detonation waves travel in both directions, away from ignition point.

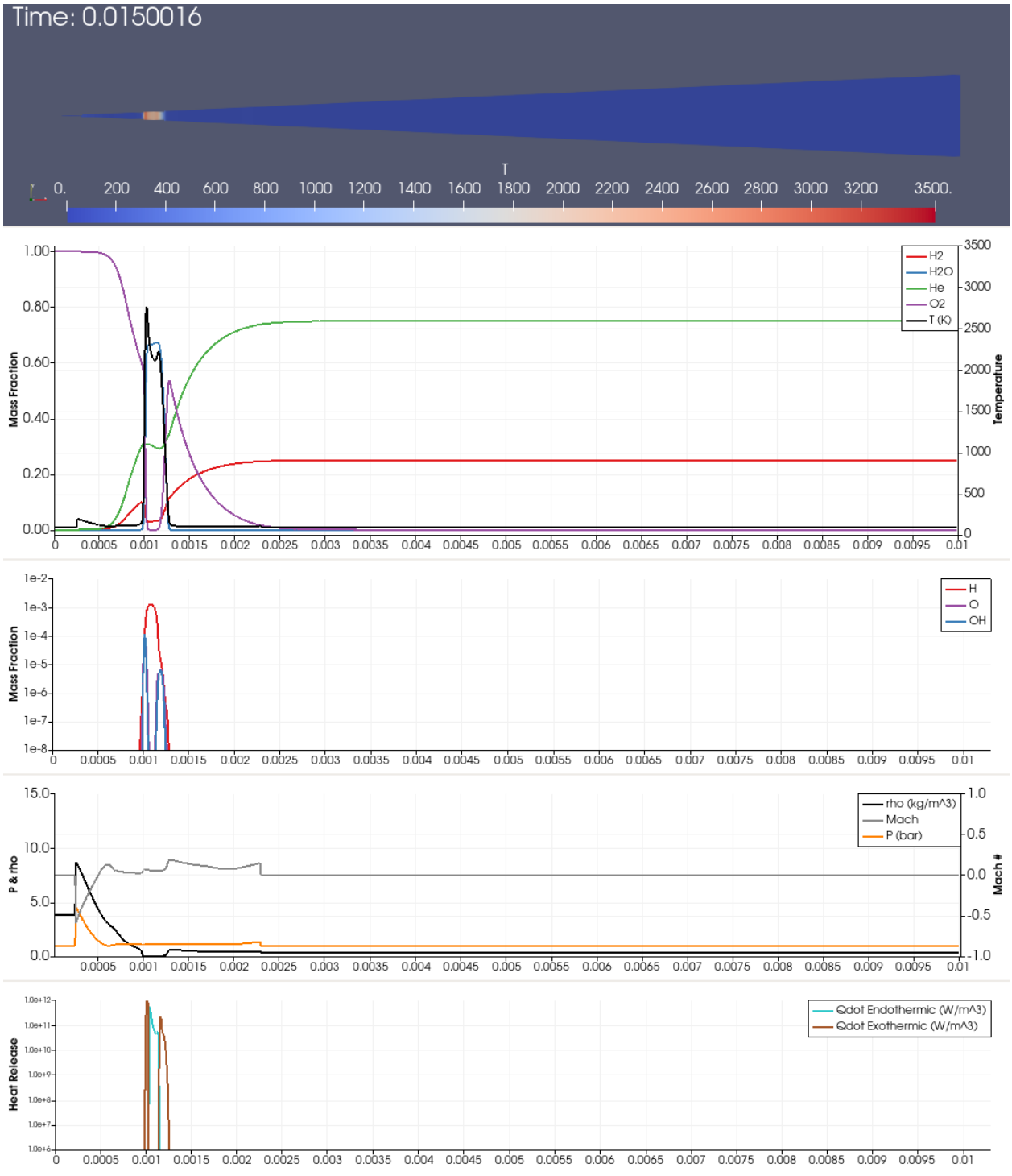

Figure 5.15: Six-step chemistry: The inner flame becomes stationary due to increased diffusion.

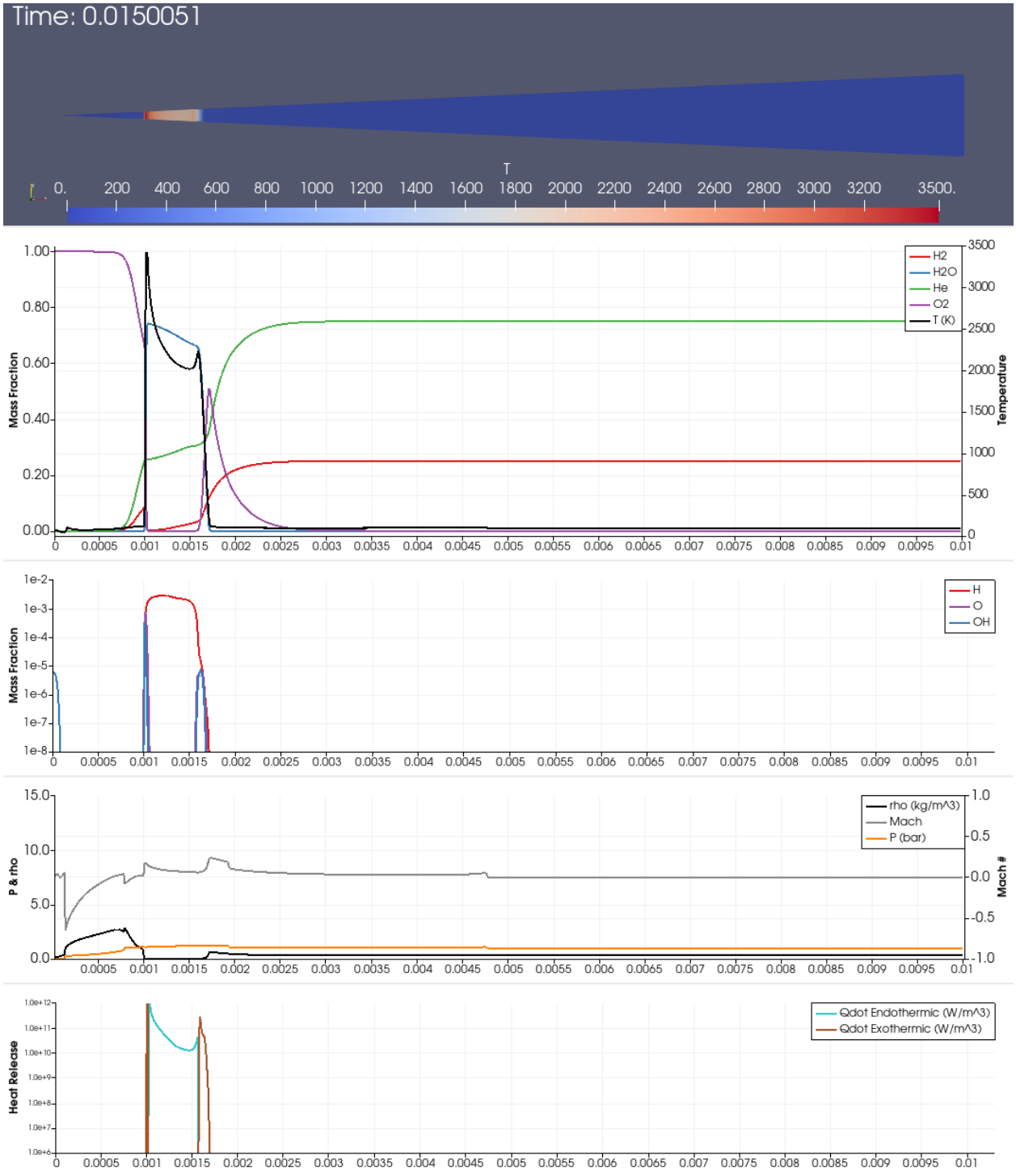

Figure 5.16: Six-step chemistry: A maximum amount of oxidizing radicals build up within the inner premixed flame before forming a diffusion flame.

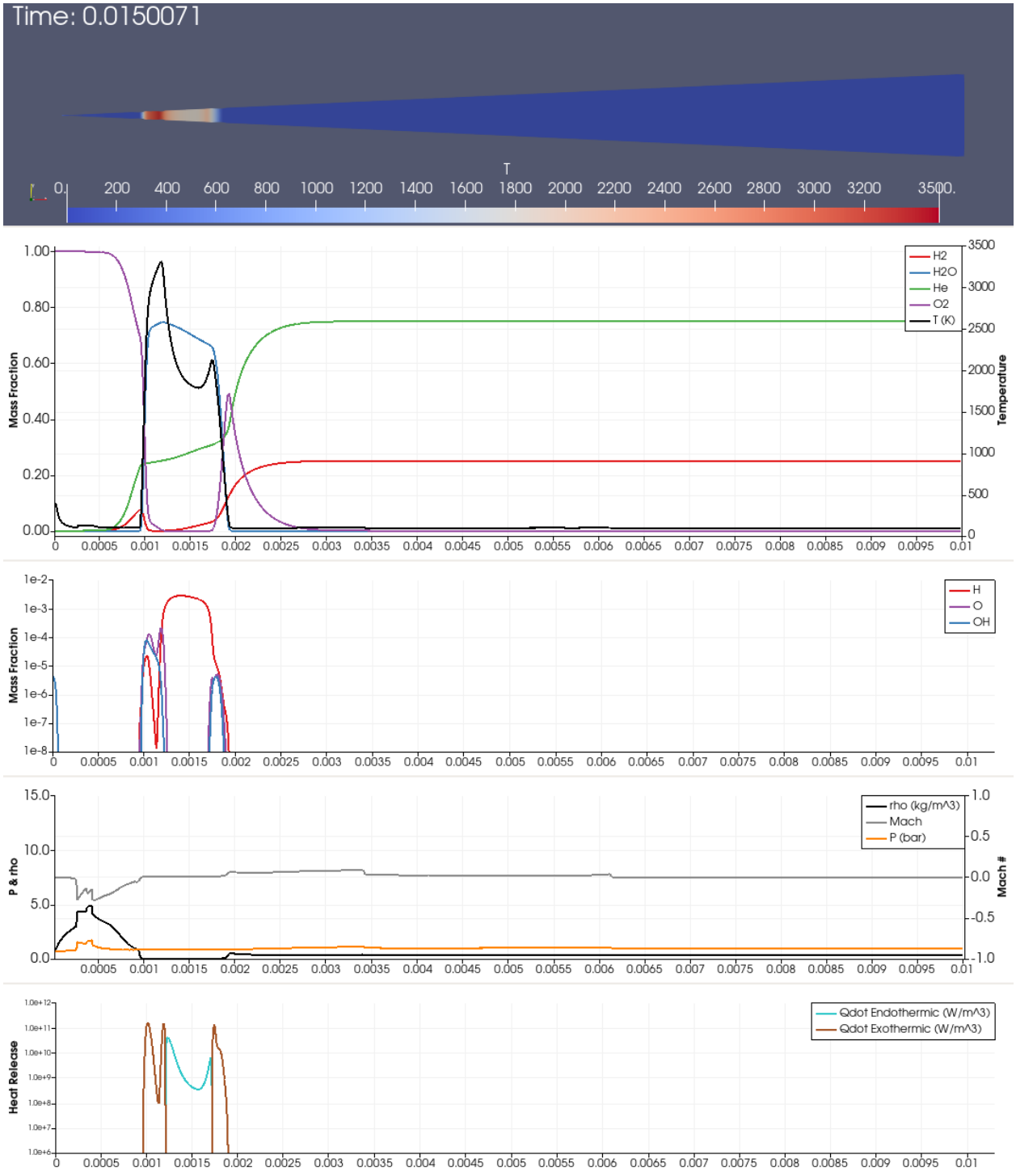

Figure 5.17: Six-step chemistry: Diffusion flame formed when oxidizing radicals spill into the hot region.

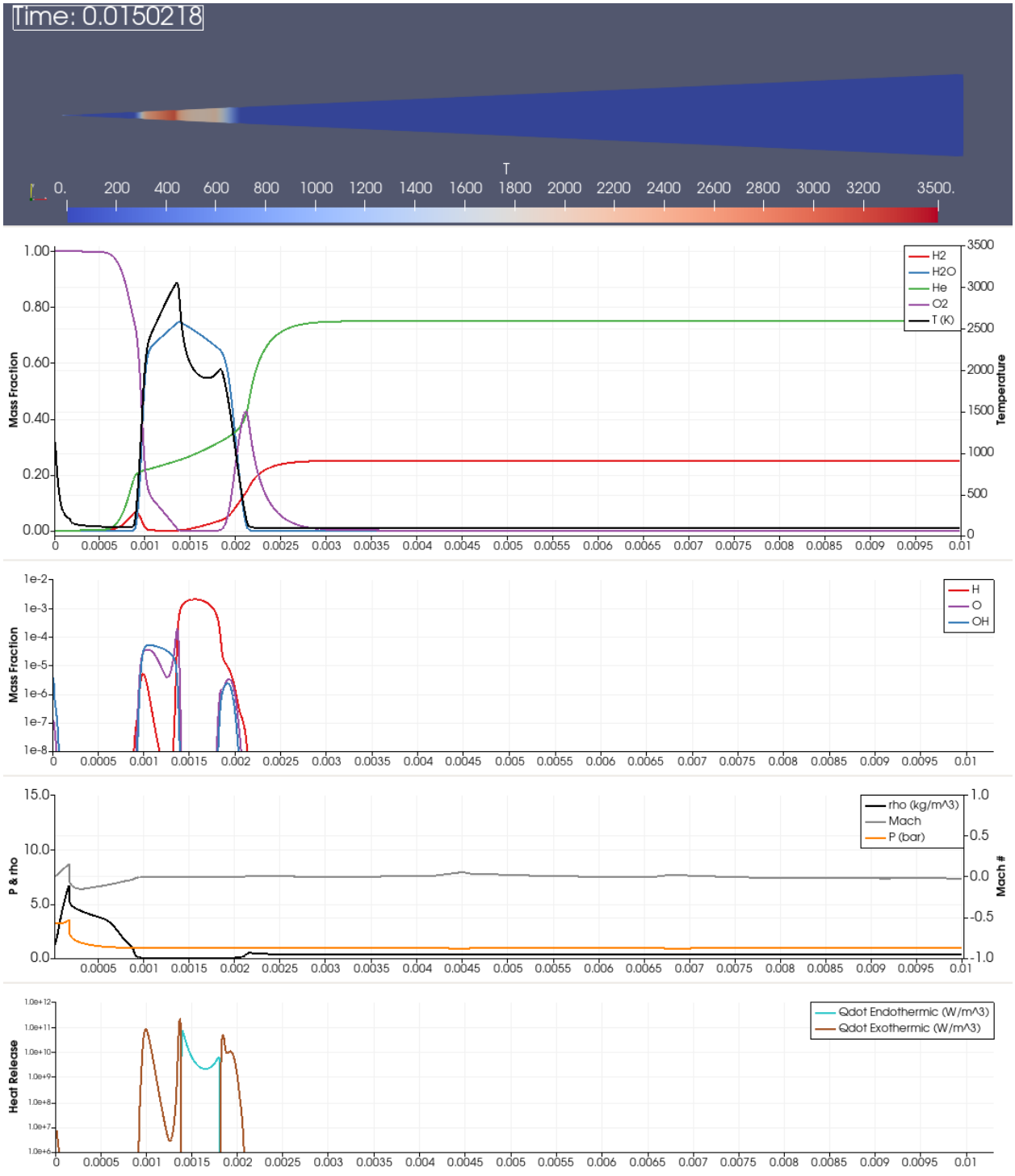

Figure 5.18: Six-step chemistry: Stabilization of flame formation. Two premixed flames are situated on either side of a diffusion flame. The peak temperature location matches the diffusion flame placement leading combustion in to pseudo-steady-state behavior.

5.3.3 Pseudo-Steady Combustion

The pseudo-steady combustion phase is characterized by the relatively larger time scale of occurrence. The two premixed flames are slowly consumed during this time span with their reaction profiles diminishing and widening as well. Furthermore as combustion produces heat, the hot region expands as well. There is a transition in flame structure during this period. The outer premixed flame transitions from fuel-lean to fuel-rich leading to the extinction of the endothermic region and a local decrease in temperature. This process occurs in a flickering sort of manner. As the flame structure is perturbed by the pressure waves, the endothermic region becomes exothermic and then reverses again. Figure 5.19 on page 63 shows the pseudo-steady state combustion with both fuel-lean premixed flames. Figure 5.20 on page 64 shows pseudo-steady state combustion after the outer flame transition to fuel-rich and flickering has ceased. Note the outer inflection-point in the temperature profile is no longer present.

The bursts of combustion near the center of the oxygen gas cloud that were seen in the single-step simulation occur just as frequently in the six-step simulation. The various figures presented show the accumulation of oxygen and hydroxide radical at the domain center. This accumulation of oxidizers allow for combustion given hydrogen radicals can be transported towards the center. Figure 5.21 on page 65 shows an example of the combusting pressure spike for the six-step simulation.

Since the end consumption of the gas cloud was not resolved that end-state of six-step simulation can be seen in Figure 5.22 on page 66.

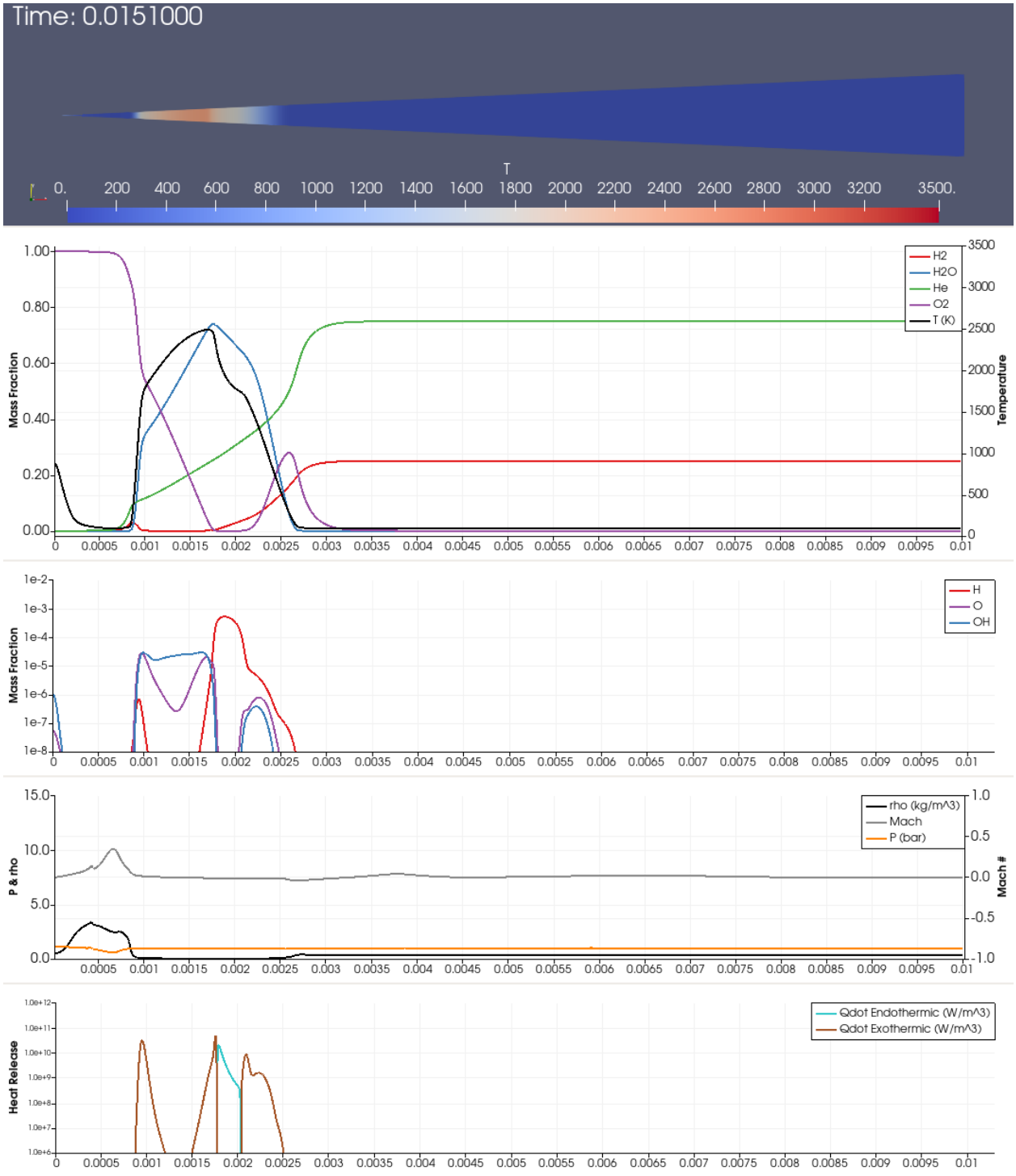

Figure 5.19: Six-step chemistry: Progression of pseudo-steady combustion with two fuel-lean premixed flames.

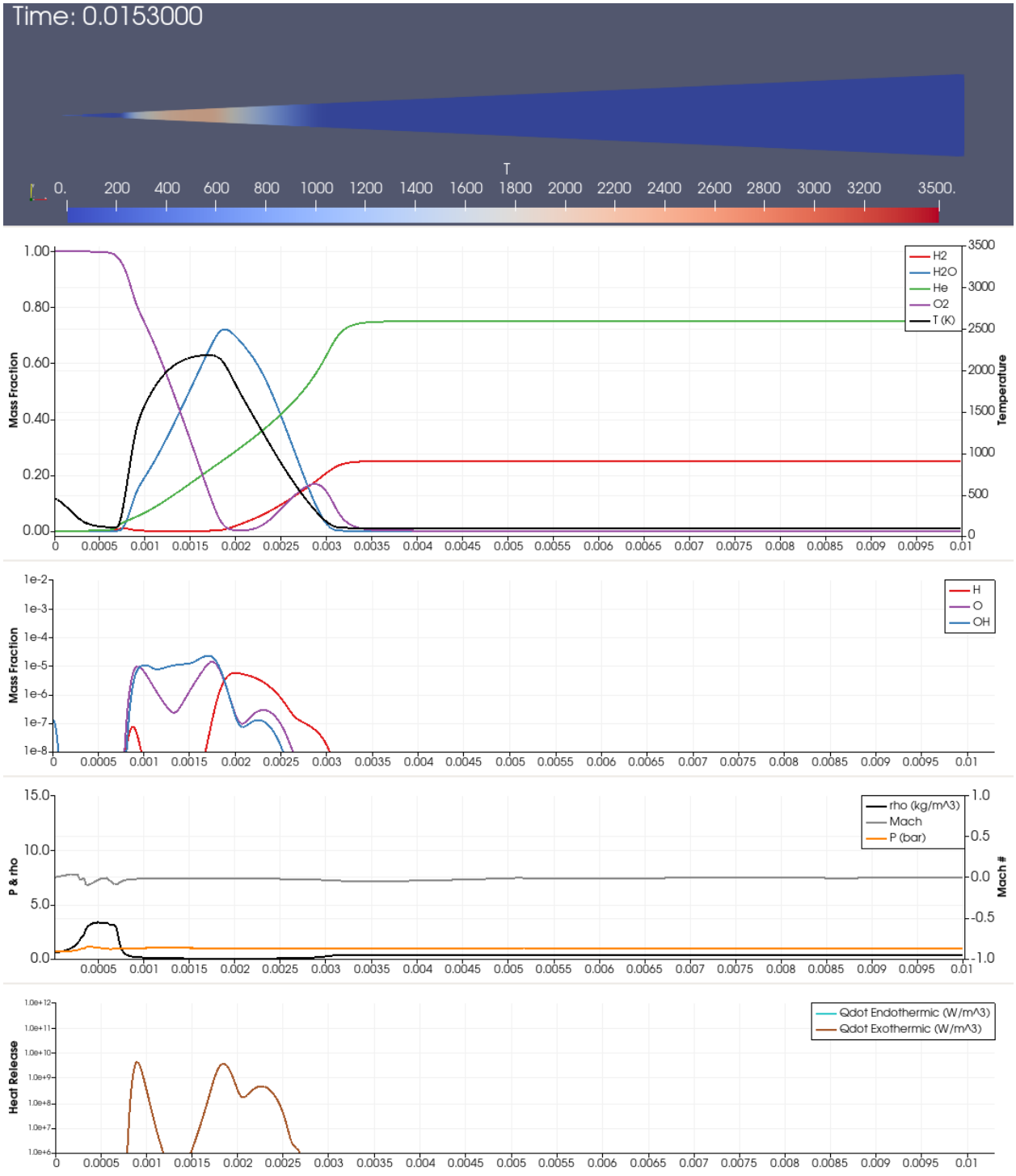

Figure 5.20: Six-step chemistry: Pseudo-steady combustion after the transition of the outer premixed flame to fuel-rich. The endothermic region is no longer present.

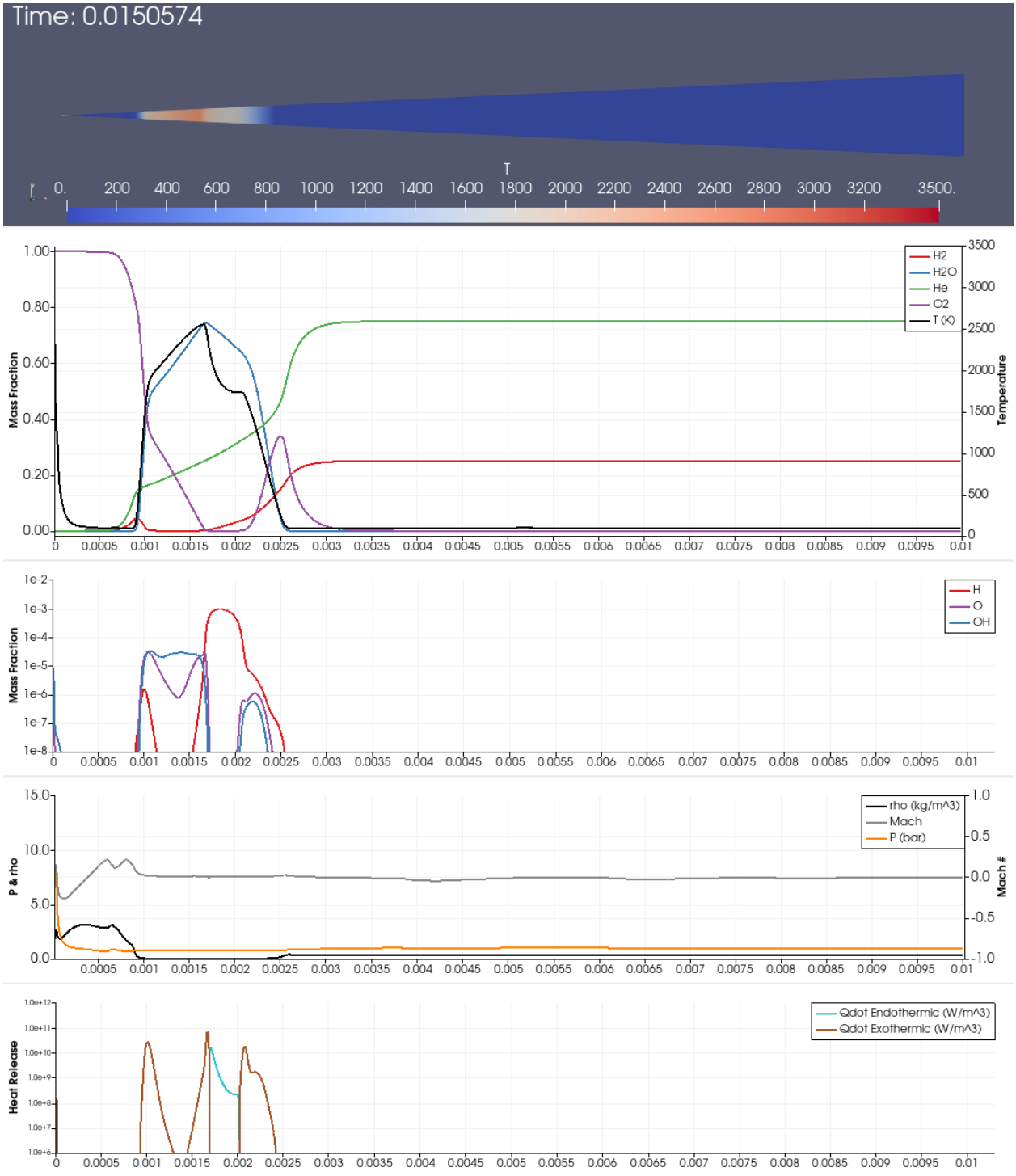

Figure 5.21: Six-step chemistry: Combustion occurs within the oxygen cloud on select occurrences of pressure spikes.

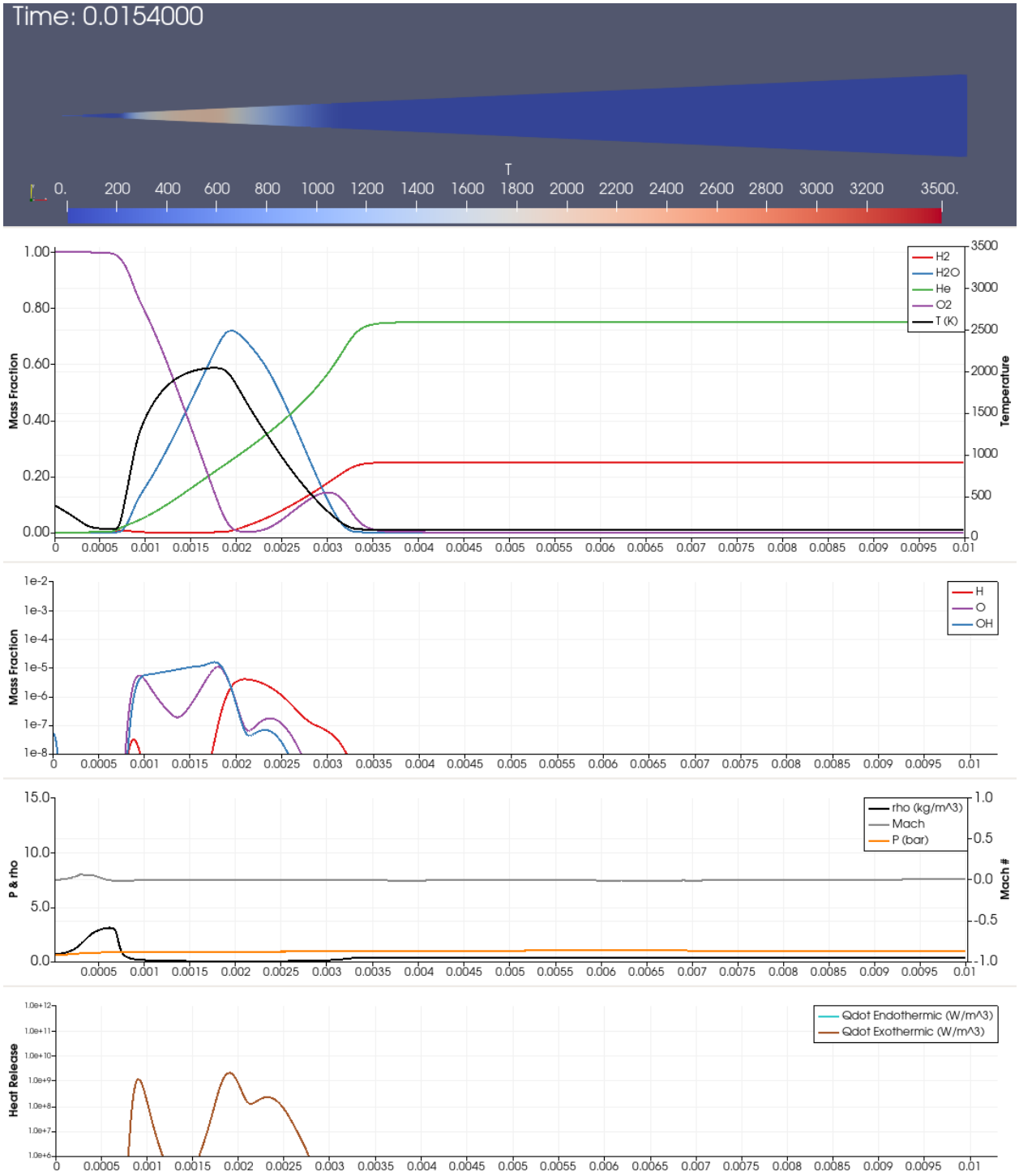

Figure 5.22: Six-step chemistry: The last computed time step.

Chapter 6

CONCLUSION

Simulations of liquid oxygen droplet in a dilute hydrogen atmosphere were successfully carried out through trial and error development of solver settings and thermo-chemical modeling. Ignition enthalpies were numerically inserted into the domain to manipulate the temperature profile and cause a sustained chemical cascade. The pressure waves cause by the ignition, and even more so the initial combustion reaction, posed the largest computational strain on the solver. The waves propagated towards the center of the domain, and the symmetry boundary conditions on the pyramidal domain acted like funnels to cause a large pressure spike to form near the origin. The extreme gradient was accounted for through small time steps of 10 or 100 picoseconds. Through flame formation and further pseudo-stable combustion, waves reflected off the compositional interface of the flame, leading to additional spikes until time progressed sufficiently for viscosity to dampen pressure profiles. Waves were not fully able to pass out of the computational domain due to the inlet-outlet boundary condition acting as a flexible wall and partially reflecting. This further exacerbated the issue of resolving waves until droplet death and near-total consumption of the simulated oxygen droplet.

Various conclusion can be made from the contrast between single-step and six-step chemistry undergoing the overall ignition and combustion processes. Inferences are established on the nature of what can be considered a flame, the steady combustion behavior, the development of concentration profiles, and the overall utility of the two chemical models. The source of the limitations in the numerical methods shared between the simulations are addressed as well.

6.1 Flames and Reaction Zones

The three exothermic locations for single-step chemistry were identified as flame regions, since heat and water were produced in these regions. In six-step chemistry, these three regions displayed more interactive behavior. The inner premixed flame zone connected to the central diffusion flame. The outer premixed flame communicated with the inner diffusion flame through and intermediate endothermic region and later a skewed exothermic region. The heat generated by the overall reaction must be due to water formation since the only other chain terminating step was recombination of oxygen radicals. This recombination recovers the heat required to cleave the oxygen gas leading to no net heat release or absorption. This prompts the question of whether water formation defines a flame or if the distribution of exothermic regions indicates a larger flame structure?

With single-step chemistry the three chain-terminating zones do not interact directly, suggesting independent flame structures. The central diffusion flame draws unconsumed reactants from the premixed flames but these extras do not effect the premixed flames by themselves. Six-step chemistry shows the sharing of radicals between flames. The outer premixed flame partially pre-ionizes hydrogen to be fed to the diffusion flame and the inner flame follows suit forming oxygen and hydroxyl radicals. The partial ionization of gases combined with the production of water implies that both chain-initiating and chain-terminating events are occurring in the central flame region. With these two requirement along with the production of heat, the central reaction zone can be deemed a flame. The inner and outer premixed reaction zones also independently localize heat production, chain-initiating chemistry, and chain-terminating chemistry. Therefore the inner and outer reactions are independent flames as well. The zone between the inner premixed region and the central flame does not have hydrogen disassociation occurring and is not a flame. The inner and central region are therefore distinct combustion zones. Furthermore the region between the central and outer reactions zones is unstable, only sometimes containing water production but always containing hydrogen disassociation. Therefore the outer premix flame and the in-

ner flame may have merged near the end of six-step simulation but without further runtime, flame distinctness is unclear.

6.2 Temperature and Concentration Profiles

Qualitatively, the temperature and major specie profiles during pseudo-steady combustion closely resemble the profiles hypothesized in Section 3.5 for both chemistry models. The profiles differ where the major products were separated by the initial ignition event becoming finite reservoirs for premixed combustion. The impact of unsteady terms could be analyzed however an analytical model for spherical counter flow diffusion must be first set up. Furthermore between the two chemistry models, the time evolution of temperature profiles towards the final are quite different. The temperature profiles conform closely to the reaction zones at all times for six-step chemistry while the temperature profile lags behind flame location in the single-step model. The six step model may better capture the molecular kinetics involved in flame formation.

6.3 Steady-Combustion Behavior

The pseudo-steady combustion behavior for both single-step and six-step chemistry match well qualitatively. Both cases show the same hypothesized profiles and flame temperatures are roughly the same, ± 100 K. Quantitative analysis of the total and instantaneous water production is needed to clarify exactly how similar the steady combustion behavior is.

6.4 Utility of Single-Step vs Six-Step Chemistry

With the qualitative analysis available, single-step chemistry is a better model for seeing steady-state combustion behavior because its produces similar results to the six-step model but with less runtime. The single step model shows weaknesses in the ignition and flame formation phases, due to excessive temperatures and chemistry-temperature decoupling. As such the six-step model is more robust for capturing the dynamics of ignition and flame formation due to their associated shorter time scales.

6.5 Simulations Limitations

The limitations of accuracy in combustion simulation results appear subtly in the foundational of equations and within the assumptions made.

6.5.1 Lewis Number Effects

The Lewis number emphasized heavily in Section 3.2 controls the relative time scales between heat and mass transfer. Simulation equations assumed in Section 2.1 assumed unity Prandtl number and unity Schmidt number, which together imply a Lewis number of unity. Considering mass is typically less mobile than energy, the Lewis number should reflect this difference. By ignoring the difference specie, temperature, density, and reaction rate profiles becomes skewed. Without a reference to point out the effects, showing how the combustion results are effected by this misappropriated assumption can be quite difficult. The effect is however quite apparent in the diffusion results.

There exists an apparent local maximum in density at ≈0.7mm and time 0.015s, as seen in Figure 5.1. This comes from the heat diffusion process struggling to keep up with the energy stealing effect of oxygen diffusion that can be seen in Equation 3.31. This results in a net temperature decrease in the vicinity of the droplet surface, at approx. 0.7mm. Since advection occurs much faster than diffusion, pressure stays isobaric at all time. Via ideal gas law coupling, for pressure to remain constant and temperature to decrease, density must increase proportionally. A density spike manifests appropriately. While this diffusion modeling limitation is not only logical and apparent, combustion modeling does not have the luxury of straight forward interpretation. The effects of the unity Lewis number may be pervasive, subtle, and unrecognizable without a suitable comparison.

6.5.2 Pressure Waves and Undamped Energy Effects

The pressure waves present in solution introduce a major limitation on runtime efficiency due to their large associated gradients. These gradients in tern require even smaller time

steps than normal. The main issue with these wave however are their apparent lack of dampening. While the momentum equation contains viscous terms that will smooth the profile over time, this actions is carried out by viscosity, which for the associated time scales is relatively small. The energy equation should contain dampening-type terms as well, but since viscosity is relatively low, neglecting viscous energy terms may be reasonable. Viscosity may be negligible but pressure waves can dampen through other mechanisms too.

The compression work term done by the bulk fluid is completely neglected in the energy equation. Considering the initial combustion event produces a high pressure locally, its reasonable to assume the pressure partially compresses domain, transforming into enthalpy during the process. This work turn is expressed as $\vec{u} \cdot \vec{\nabla} P$. As such it can be assumed that a physical pressure wave, without viscous considerations, should round off it's sharp gradient as it travels, leaving a trail of increased enthalpy in its wake. While this effect is hypothesized, it can be for sure known that the lingering of the pressure waves is a non-physical result.

6.5.3 Ideal Gas Behavior

The assumption of ideal gas behavior made for a usable model which allowed for straightforward analysis of results, especially since the pressure, temperature, and bulk density were directly correlated.

Chapter 7

RECOMMENDATIONS

7.1 Fourier Transform of the Pressure Waves

If a dominant frequency of internal droplet waves exists, it can be picked up via a time Fourier transform at a fixed point. Dominant frequencies may have implications for combustion acoustics.

7.2 Symmetry Condition Relaxation

The spherical symmetry condition may have caused longer numerical runtimes than needed. Counter-intuitively, by removing a degree of symmetry and establishing a spherically-wedge-shaped domain, solutions may be achieved in faster time. Without the nozzling effect of the one-dimensional domain, the pressure spikes seen in solutions will not exist. The solver residuals and time-steps may not need to be so small then.

7.3 Alternative Six Step Chemistry Scheme

For an alternate six-step chemistry scheme that can be used in simulations, see: "Theory of a Hydrogen-Oxygen Diffusion Flame, Part I: Profiles from a Large Damkohler Number Model" R.A. Allison & J.F. Clark 1979. The work presented in Allison and Clark's article establishes the accuracy of a reduced-order chemistry model, which this project has neglected.

7.4 Wave-Absorbing Boundary Condition

For a mathematical formulation of a more realistic boundary condition on the exterior of the computational domain, see: "Accurate Boundary Conditions for Multicomponent Reactive Flows" M. Baum, T. Poinsot, & D. Thevenint: 1993. While not discussed heavily, simulations

in this project show wave reflections on the inlet-outlet boundary condition. Since the outer boundary represents an imaginary cut, reflections should not be present.

7.5 Mesh Modifications

The mesh could be modified so that cell density is coarse near center of droplet and exterior and dense cells from 1mm to 3mm, where most of the combustion dynamics occur. Placing more cells were needed and less elsewhere will likely increase computational efficiency

7.6 Solver Modifications

Time-steps can be calculated faster by increasing the number of PIMPLE outer loops and solving for relative-tolerance residuals, instead of the absolute-tolerance scheme used in this project. This will result in a more FLUENT-type of convergence pattern. Futhermore increasing the limit on number of steps within the chemistry ODE solver from 1e5 to 1e6, or maybe even 1e7, may provide more flexible solution schemes.

7.7 Thermophysical Modifications

By implementing the phase models and Lewis numbers from Section 3.1, realistic combustion and evaporation simulation may be possible.

7.8 Including Energy Dissipation Terms

The enthalpy transport equation is missing irreversible terms like $\tau : \vec{\nabla}\vec{u}$. Including these terms in the energy equation may put decrease solver stability but would greatly dampen the ignition waves which limit simulation time steps. Additionally, including these terms were add feasibility to simulation data.

7.9 Replacing the Energy Equation for Gibbs Transport

Replace the Fickian diffusion model for the Maxwellian model because Fickian diffusion coefficients have not been experimentally recorded for the low temperature values/ extreme

temperature gradients that are present in H2-LOX combustion. The Maxwellian model of diffusion relates the diffusion coefficients to the Gibbs potential via kinetic theory and can therefore be calculated. Viscosity and conductivity can be related to kinetic theory as well. Perhaps even include the surface tension expression in the deviatoric stress, since surface tension can be expressed as a Gibbs energy minimizer. To solve for Gibbs energy, replace the energy equation for Gibbs transport. Unfortunately the entropy transport equation would be needed as well to fully resolve the temperature. These steps entail a large project.

BIBLIOGRAPHY

[1] Jackson I. Ito. Propellant injection systems and processes. In Vigor Yang, editor, Progress in Astronautics and Aeronautics : Liquid Rocket Thrust Chambers. American Institute of Aeronautics and Astronautics, Reston, US, 2000.

[2] Jim Ponzo. Overview of liquid rocket engine stability. Presented at the University of Washington, May 2018.

[3] A. Richard Seabass, editor. Modern Engineering for Design of Liquid-Propellant Rocket Engines. American Institute of Aeronautics and Astronautics, Washington D.C., 1992.

[4] F. Moukalled, L. Mangani, and M. Darwish. The Finite Volume Method in Computational Fluid Dynamics. Springer, Heidelberg, 2016.

[5] Tobias Holtzmann. Mathematics, Numerics, Derivations and OpenFOAM(R). Holzmann CFD, Leoben, 4 edition, 2016.

[6] Christopher J. Greenshields. OpenFOAM Programmer's Guide version 5.0. OpenFOAM Foundation Ltd., 2017.

[7] Irvin Glassman and Richard A. Yetter. Combustion. Academic Press, Oxford, 4 edition, 2008.

[8] Peter Kidwelly, editor. Detailed and Global Chemical Kinetics Model for Hydrogen. Lawrence Livermore National Lab., CA, 1995.

[9] J. Kestin, K. Knierim, E. A. Mason, B. Najafi, S. T. Ro, and M. Waldman. Equilibrium and transport properties of the noble gases and their mixtures at low density. Journal of Physical and Chemical Reference Data, 13(1):229–303, 1984.

[10] M. Faraday. The Chemical History of a Candle. Dover, 2002.

[11] R. Byron Bird, Warren E. Stewart, and Edwin N. Lightfoot. Transport Phenomena. Wiley, New York, 1960.

[12] Christopher J. Greenshields. OpenFOAM User Guide version 5.0. OpenFOAM Foundation Ltd., 2017.

[13] Ross Taylor and R. Krishna. Multicomponent Mass Transfer. Wiley, New York, 1993.

[14] Moshe Matalon. Lecture 10 diffusion flames, Summer 2013.

[15] H. G. Weller, G. Tabor, H. Jasak, and C. Fureby. A tensorial approach to computational continuum mechanics using object-oriented techniques. Computers in Physics, 12(6):620–631, 1998.

[16] Gary A. Sod. A survey of several finite difference methods for systems of nonlinear hyperbolic conservations laws. Journal of Computational Physics, 27(1):1–31, 1978.

[17] CFD Direct. Energy equation in openfoam.

[18] P.K. Sweby. High resolution schemes using flux limiters for hyperbolic conservation laws. SIAM Journal on Numerical Analysis, 21:995–1011, 1984.

[19] Charles Hirsch. Numerical Computation of Internal and External Flows, volume 1. Wiley, Chichester, 2001.

[20] R. Courant, K. Friedrichs, and H. Lewy. On the partial difference equations of mathematical physics. IBM Journal of Research and Development, 11(2):215–234, March 1967.

[21] Utkarsh Ayachit. The Paraview Guide. Kitware Inc., 2016.

Appendix A

APPENDIX A: REACTINGIGNFOAM CODE

The solver reactingIgnFoam is an implementation of reactingFoam that borrows elements from the engineFoam library. As such the combustions libraries mimic those found in either XiFoam or dieselFoam, which model internal combustion engines. The code quoted here is from OpenFOAM v5.0 and will only work with this version. To implement this code in another OpenFOAM version, reactingFoam can be modified by adding the changed pieces of code, highlighted in yellow.

A.1 reactingIgnFoam.C

```
/*---------------------------------------------------------------------------*\
=========                 |
\\      /  F ield         | OpenFOAM: The Open Source CFD Toolbox
\\    /   O peration     |
\\  /    A nd           | Copyright (C) 2011-2017 OpenFOAM Foundation
\\/     M anipulation  |
-------------------------------------------------------------------------------
License
This file is part of OpenFOAM.

OpenFOAM is free software: you can redistribute it and/or modify it
under the terms of the GNU General Public License as published by
the Free Software Foundation, either version 3 of the License, or
(at your option) any later version.
```

```
OpenFOAM is distributed in the hope that it will be useful, but WITHOUT
ANY WARRANTY; without even the implied warranty of MERCHANTABILITY or
FITNESS FOR A PARTICULAR PURPOSE. See the GNU General Public License
for more details.

You should have received a copy of the GNU General Public License
along with OpenFOAM. If not, see <http://www.gnu.org/licenses/>.

Application
reactingFoam

Description
Solver for combustion with chemical reactions.

\*---------------------------------------------------------------------------*/

#include "fvCFD.H"
#include "turbulentFluidThermoModel.H"
#include "psiCombustionModel.H"
#include "multivariateScheme.H"
 #include "ignition.H"
#include "pimpleControl.H"
#include "pressureControl.H"
#include "fvOptions.H"
#include "localEulerDdtScheme.H"
#include "fvcSmooth.H"

// * * * * * * * * * * * * * * * * * * * * * * * * * * * * * * * * * * * * * * * //
```

```
int main(int argc, char *argv[])
{
    #include "postProcess.H"

    #include "setRootCase.H"
    #include "createTime.H"
    #include "createMesh.H"
    #include "createControl.H"
    #include "createTimeControls.H"
    #include "initContinuityErrs.H"
     #include "readCombustionProperties.H"
    #include "createFields.H"
    #include "createFieldRefs.H"
    #include "createFvOptions.H"

    turbulence->validate();

    if (!LTS)
    {
        #include "compressibleCourantNo.H"
        #include "setInitialDeltaT.H"
    }

    // * * * * * * * * * * * * * * * * * * * * * * * * * * * * * * * * * * * * * //

    Info<< "\nStarting time loop\n" << endl;

    while (runTime.run())
    {
```

```
#include "readTimeControls.H"

if (LTS)
{
    #include "setRDeltaT.H"
}
else
{
    #include "compressibleCourantNo.H"
    #include "setDeltaT.H"
}

runTime++;

Info<< "Time = " << runTime.timeName() << nl << endl;

#include "rhoEqn.H"

while (pimple.loop())
{
    #include "UEqn.H"
    #include "YEqn.H"
     #include "ignite.H"
    #include "EEqn.H"

    // --- Pressure corrector loop
    while (pimple.correct())
    {
        if (pimple.consistent())
```

```
            {
                #include "pcEqn.H"
            }
            else
            {
                #include "pEqn.H"
            }
        }

        if (pimple.turbCorr())
        {
            turbulence->correct();
        }
    }

    rho = thermo.rho();

    runTime.write();

    Info<< "ExecutionTime = " << runTime.elapsedCpuTime() << " s"
    << "  ClockTime = " << runTime.elapsedClockTime() << " s"
    << nl << endl;
}

Info<< "End\n" << endl;

return 0;
}
```

```
// ********************************************************************************* //
```

A.2 ignite.H

```
if (ign.ignited())
  {
     volScalarField& he = thermo.he();
     forAll(ign.sites(), i)
        {
           const ignitionSite& ignSite = ign.sites()[i];
           if (ignSite.igniting())
              {
              forAll(ignSite.cells(), icelli)
              {
                 label ignCell = ignSite.cells()[icelli];
                 if (T[ignCell] < 2000.0)
              {
              Info << "Igniting cell " << ignCell << endl;
              scalar magH = mag(he[ignCell]);
              he[ignCell] += ignSite.strength()*magH;
           }
        }
     }
  }
}
```

A.3 Make/options

```
EXE_INC = \
```

```
-I$(LIB_SRC)/finiteVolume/lnInclude \
-I$(LIB_SRC)/meshTools/lnInclude \
-I$(LIB_SRC)/sampling/lnInclude \
-I$(LIB_SRC)/TurbulenceModels/turbulenceModels/lnInclude \
-I$(LIB_SRC)/TurbulenceModels/compressible/lnInclude \
-I$(LIB_SRC)/thermophysicalModels/specie/lnInclude \
-I$(LIB_SRC)/thermophysicalModels/reactionThermo/lnInclude \
-I$(LIB_SRC)/transportModels/compressible/lnInclude \
-I$(LIB_SRC)/thermophysicalModels/basic/lnInclude \
-I$(LIB_SRC)/thermophysicalModels/chemistryModel/lnInclude \
-I$(LIB_SRC)/ODE/lnInclude \
-I$(LIB_SRC)/combustionModels/lnInclude \
-I$(LIB_SRC)/engine/lnInclude

EXE_LIBS = \
-lfiniteVolume \
-lfvOptions \
-lmeshTools \
-lsampling \
-lturbulenceModels \
-lcompressibleTurbulenceModels \
-lreactionThermophysicalModels \
-lspecie \
-lcompressibleTransportModels \
-lfluidThermophysicalModels \
-lchemistryModel \
-lODE \
-lcombustionModels \
-lengine
```